Combining In Situ Synchrotron X-Ray Diffraction and Absorption Techniques with Transmission Electron Microscopy to Study the Origin of Thermal Instability in Overcharged Cathode Materials for Lithium-Ion Batteries

Kyung-Wan Nam, Seong-Min Bak, Enyuan Hu, Xiqian Yu, Youngning Zhou, Xiaojian Wang, Lijun Wu, Yimei Zhu, Kyung-Yoon Chung, and Xiao-Qing Yang**

The thermal instability of the cathode materials in lithium-ion batteries is an important safety issue, requiring the incorporation of several approaches to prevent thermal runaway and combustion. Systematic studies, using combined well-defined in situ techniques, are crucial to obtaining in-depth understanding of the structural origin of this thermal instability in overcharged cathode materials. Here time-resolved X-ray diffraction, X-ray absorption, mass spectroscopy, and high-resolution transmission electron microscopy during heating are combined to detail the structural changes in overcharged $Li_xNi_{0.8}Co_{0.15}Al_{0.05}O_2$ and $Li_xNi_{1/3}Co_{1/3}Mn_{1/3}O_2$ cathode materials. By employing these several techniques in concert, various aspects of the structural changes are investigated in these two materials at an overcharged state; these include differences in phase-distribution after overcharge, phase nucleation and propagation during heating, the preferred atomic sites and migration paths of Ni, Co, and Mn, and their individual contributions to thermal stability, together with measuring the oxygen release that accompanies these structural changes. These results provide valuable guidance for developing new cathode materials with improved safety characteristics.

1. Introduction

Lithium-ion batteries, after dominating the market for several years as rechargeable power-sources for cellphones, laptop computers, and other mobile computing and communication devices, are now expanding their application to power sources for electric vehicles (EVs), hybrid electric vehicles (HEVs), and plug-in hybrid electric vehicles (PHEVs). However, the development of new electrode materials for the next generation of lithium-ion batteries for EV applications, with requirements for higher energy-density, longer life, and better safety[1–3] needs further systematic studies of the structural changes of the electrode materials during charge–discharge cycling, aging, and thermal decomposition. Different types of in situ diagnostic tools must be advanced and applied in such studies to provide essential knowledge for formulating new electrode materials, as well as for improving performance in today's commercial lithium-ion batteries. Already, various in situ and ex situ spectroscopic techniques have been employed to investigate lithium-ion battery materials, including X-ray- and neutron-diffraction,[4–12] X-ray absorption spectroscopy (XAS),[13–19] Fourier transform-infrared (FTIR) spectroscopy,[20–22] Raman spectroscopy,[23–25] mass spectroscopy (MS),[26–28] and nuclear magnetic resonance (NMR).[29–31] Recently, in situ transmission X-ray microscopy (TXM) was used to monitor morphological evolution during battery cycling.[32,33] The advantage of this technique is the ability to monitor in situ the volume change of individual particles of the electrodes of lithium-ion cells during the cycles of charge–discharge. On the other hand, the disadvantages are the poor spatial resolution and lack of microscopic structural information. Higher resolution data on morphology recently was obtained via scanning electron microscopy (SEM), down to 1 nm spatial resolution, during lithium uptake and release inside a working battery electrode.[34] The transmission electron microscopy (TEM) is another advanced technique, however, due to the limitations on obtaining a high vacuum, most such studies on Li-ion batteries are carried out ex situ. In situ TEM recently was established to study Li-ion batteries during electrochemical charging using a low-vapor-pressure ionic liquid as an electrolyte and a single SnO_2 nanowire as the anode.[35]

Dr. K.-W. Nam, S.-M. Bak, E.-Y. Hu, Dr. X.-Q. Yu, Dr. Y.-N. Zhou, Dr. X. J. Wang, Dr. X.-Q. Yang
Chemistry Department
Brookhaven National Laboratory
Upton, NY 11973, USA
E-mail: xyang@bnl.gov

Dr. L. Wu, Dr. Y. Zhu
Condensed Matter Physics and Material Science Department
Brookhaven National Laboratory
Upton, NY 11973, USA
E-mail: ljwu@bnl.gov

S.-M. Bak, Dr. K.-Y. Chung
Center for Energy Convergence
Green City Technology Institute
Korea Institute of Science and Technology
Seoul, 136-791, Korea

DOI: 10.1002/adfm.201200693

That in situ experiment revealed a reaction front containing a high density of mobile dislocations propagating progressively along the nanowire, causing the nanowire to swell, elongate, and spiral upward. This novel study offered exciting real-time images of the microscopic structural changes in the single-nanowire SnO_2 anode during lithiation for a special designed lithium-battery cell; accordingly, more research and development is being actively pursued to improve resolution and to generate in situ structural information in cells operating under conditions close to those in real commercial Li-ion cells.

In the field of materials research, high energy-density, low-cost Ni-based layer-structured $LiNi_{0.8}Co_{0.15}Al_{0.05}O_2$ and $LiNi_{1/3}Co_{1/3}Mn_{1/3}O_2$ are promising cathode materials for the new generation of Li-ion batteries, especially as power sources for EV and HEV applications.[36,37] Recently, several leading lithium-ion battery manufacturers in Japan and Korea announced their successful formulations of high-capacity (3.2 and 3.6 A h) 18650 Li-ion cells using a Ni-based cathode material, similar to $LiNi_{0.8}Co_{0.15}Al_{0.05}O_2$. This advance demonstrated the great potential of this type of materials, so warranting an in-depth study of these materials that will undoubtedly provide important information in formulating high-capacity cells. However, one troubling issue in using Ni-rich cathode materials is their thermal instability, which might jeopardize safety during thermal runaway – a major concern for EVs and PHEVs. Reportedly, at highly delithiated states (overcharged), the reduction of Ni^{4+} during heating releases oxygen that can accelerate severe thermal runaway by reacting with the electrolyte before leading to catastrophic failure of the battery.[38–41] In this article, we discuss the initial results of our newly developed simultaneous time-resolved XRD (TR-XRD) and mass spectroscopy (MS) work at beamline X7B of the National Synchrotron Light Source (NSLS) that provides clear evidence for the co-related oxygen release and phase transitions for overcharged $Li_xNi_{0.8}Co_{0.15}Al_{0.05}O_2$ samples during heating. Another problem with these batteries is the rock-salt structured NiO formed at the surface of the electrode through the reduction of Ni^{4+}, which raises the impedance of the cathode during cycling and degrades the battery's cycling capacity.[42–45] Therefore, more thermally stable cathode materials with reduced concentrations of Ni, e.g., $LiNi_{1/3}Co_{1/3}Mn_{1/3}O_2$, were developed.[46,47] Thermogravimetric analysis (TGA) revealed that $Li_{0.55}Ni_{1/3}Co_{1.3}Mn_{1/3}O_2$ powders, in comparison with $Li_{0.45}Ni_{0.8}Co_{0.15}Al_{0.05}O_2$ powders, start to release oxygen at higher temperatures, and consequently lose much less oxygen.[39,48] Differential scanning calorimetry (DSC) also shows that the former has higher onset temperature and lower heat generation than the latter, indicating much better thermal stability. Unfortunately, this invaluable higher thermal stability is obtained at the expense of energy density. Recently, a concentration-gradient cathode material based on layered Li-Ni-Co-Mn oxides showed not only high energy density but also excellent cycling and safety characteristics.[49] In situ high-temperature XRD,[50–52] in situ TR-XRD,[53–55] XAS,[56–59] and mass spectroscopy combined withTGA/DSC,[60,61] has been utilized to study phase-transition behavior during heating and thermal decomposition; the results revealed the release of oxygen from the Ni-based layered cathodes to be associated with several structural transformations, including *R-3m* (layered) → *Fd3m* (spinel) → *Fm3m* (rock-salt) transitions, especially with the last one to the rock-salt structure. Another technique, viz., transmission electron microscopy (TEM), can provide high-spatial resolution data both on local structure and chemical content during phase transformation;[62–65] to date, this approach has not been widely applied for thermal stability studies on overcharged cathode materials. Unfortunately, most of these powerful in situ and ex situ characterization techniques for studying structural changes through the entire electrodes have been used individually, and thus can only detail one aspect of the problem at a time, rather than a complete picture of the microscopic structural changes. Therefore, they fall short in answering questions such as where and how the new structure nucleates and propagates, as well as how each element contributes to the thermal stability of the materials during thermal decomposition. Here, we discuss our new systematic study on the structural changes of two important cathode materials, $LiNi_{0.8}Co_{0.15}Al_{0.05}O_2$ and $LiNi_{1/3}Co_{1/3}Mn_{1/3}O_2$ at overcharged states during heating. These studies were carried out by using a combination of in situ synchrotron-based time-resolved X-ray diffraction (TR-XRD) and mass spectroscopy (MS), X-ray absorption spectroscopy (XAS), and in situ TEM. **Scheme 1** depicts these in situ techniques as we applied them to studying the same batch of samples with similar electrochemical histories and heating conditions. The TR-XRD results represent a road map of the average structural changes for the phase transitions: the MS is used to monitor the oxygen-releasing behavior, the results from the XAS show the local

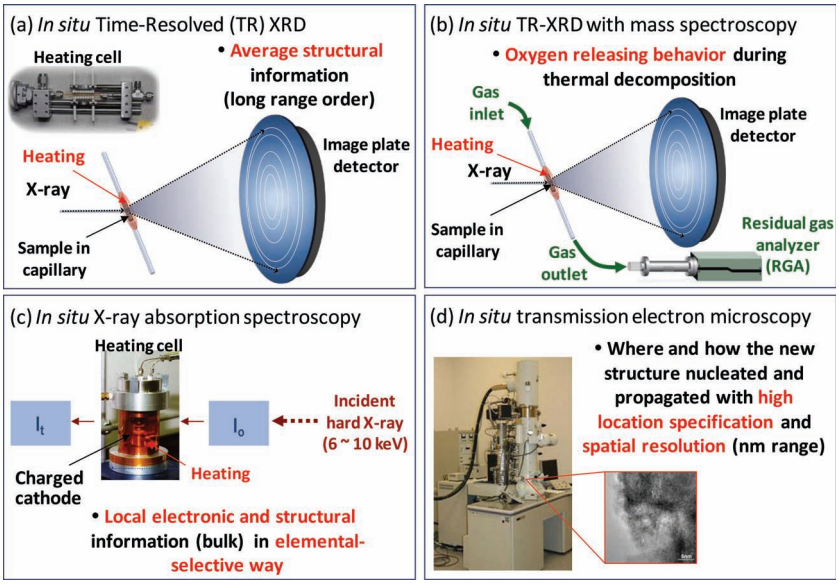

Scheme 1. Various in situ techniques used in this study for characterizing structural changes caused by thermal decomposition in overcharged cathode materials during heating: a) in situ time-resolved X-ray diffraction (TR-XRD); b) combined in situ TR-XRD and mass spectroscopy (MS); c) in situ X-ray absorption spectroscopy; and d) in situ transmission electron microscopy (TEM).

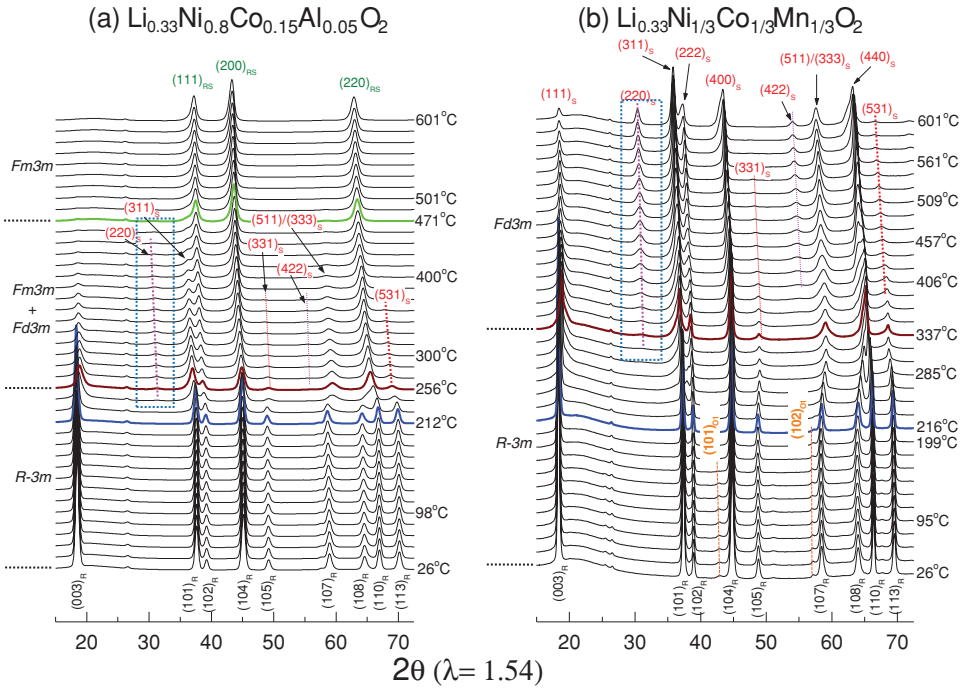

Figure 1. Time-resolved (TR) XRD patterns of the overcharged a) $Li_{0.33}Ni_{0.8}Co_{0.15}Al_{0.05}O_2$, and,b) $Li_{0.33}Ni_{1/3}Co_{1/3}Mn_{1/3}O_2$ during heating up to 600 °C. The overcharged cathode samples sealed in quartz capillaries were heated from 25 to 600 °C for 4 h during the TR-XRD measurement (heating rate = 2.4 °C min^{-1}). The subscripts R, S, and RS denote rhombohedral, spinel, and rock-salt structure, respectively. The subscript O1 represents CdI_2-type MO_2 (M = Ni, Co and Mn) structure. The expanded $(220)_S$ peak regions. Boxed regions in (a,b) are plotted in the Supporting Information (Figure S3).

structural changes and evolution surrounding certain transition metal elements (Ni, Co, Mn) and their oxidation states, while the in situ TEM results offer detailed pictures about where the nucleation of the new phases occurs under overcharged states, and how the new phases propagate during heating. The combination of these different in situ techniques provides a unique opportunity to understand the microscopic structural origin of the thermal instability due to the overcharge. It also offers a useful guidance in developing new in situ diagnostic tools for research on battery materials.

2. In Situ Time-Resolved X-Ray Diffraction (TR-XRD)

XRD is a proven powerful technique to study crystal structure and phase transformations. For detailing the thermal instability of overcharged cathode materials, in situ XRD affords us a good roadmap on the average structural changes through phase transitions during thermal decomposition, which is crucial to understanding the thermal stability behavior of cathode materials. **Figure 1**a,b show a series of TR-XRD patterns of the charged $Li_xNi_{0.8}Co_{0.15}Al_{0.05}O_2$ (i.e., Li_xNCA) and $Li_xNi_{1/3}Co_{1/3}Mn_{1/3}O_2$ (i.e., Li_xNCM) electrodes with $x = 0.33$ that we collected continuously during heating up to 600 °C in the absence of the electrolyte. It is widely accepted in lithium battery research and industrial community that the fully charged state for layer structured materials such as Li_xNCA and Li_xNCM is usually defined as $x = 0.5$, and any such material with x-value less than 0.5 is considered as overcharged. The lithium contents were estimated by the charge passed in the half-cell, assuming 100% columbic efficiency; the galvanostatic charging profiles of the two electrodes are shown in the Supporting Information (Figure S1). The XRD pattern of the overcharged $Li_{0.33}NCA$ at room temperature in Figure 1a reveals shows a rhombohedral structure (*R-3m*) wherein the phase transition from this phase to the disordered spinel (*Fd3m*) phase starts at about 212°C (marked on Figure 1a), and is completed at about 256 °C. The intensity ratio of the $(003)_R$ and $(104)_R$ peaks of the rhombohedral structure in this $Li_{0.33}NCA$ sample decreases with increasing temperature. This finding indicates that a considerable number of cations have migrated from the transition metal layer to the Li layer upon heating, as is discussed in detail later. The phase transition from spinel to rock-salt phase starts at about 256 °C and finishes at about 471 °C, as indicated by the decrease in intensity of the spinel's $(311)_S$ and $(511)_S$ peaks and consistent with the previous results.[53] On the other hand, the TR-XRD for the $Li_{0.33}NCM$ sample in Figure 1b shows considerably different phase-transition behaviors compared to the $Li_{0.33}NCA$ sample. Although the rhombohedral phase remains the dominant one, a new phase appeared in the overcharged $Li_{0.33}NCM$ sample, as is apparent from the additional weak peaks that are indexed with a CdI_2-type structure[66,67] (denoted as the O1 phase, the details about which are described in Supporting Information S2 and in the literature[66,67]). Others have reported the existence of O1 phase in highly delithiated $Li_xNi_{1/3}Co_{1/3}Mn_{1/3}O_2$.[68] The

phase transition from the rhombohedral-phase to the spinel one starts at about 216 °C and is completed at about 337 °C, which is significantly higher than the corresponding values for the $Li_{0.33}$NCA sample. When heated to above 400 °C, the spinel structure of the $Li_{0.33}$NCM undergoes another phase transition, as indicated by the gradually increasing intensities of the $(220)_S$ and $(422)_S$ peaks with rising temperature. As will be discussed in more detail later, XRD analysis highlights that the increased intensities of $(220)_S$ and $(422)_S$ peaks are due to the increased partial occupancy of the transition metals (Ni, Co, and Mn) at the tetrahedral sites (Wyckoff position 8a in *Fd3m* symmetry). For convenience, we refer to this kind of structure as the Co_3O_4-type spinel (the Co site can be occupied by other transition metals, such as Ni and Mn, in the materials studied here), to distinguish it from the LiM_2O_4-type spinel structure, in which no transition metals occupy the tetrahedral sites. The formation of this Co_3O_4-type spinel structure pushes the phase transition to the rock-salt structure at a higher temperature.

Figure 1a reveals that the intensity of the $(220)_S$ peak for the $Li_{0.33}$NCA sample started to increase at about 235 °C and reached a maximum at about 300 °C, then declining to a very low level at 500 °C. More details on these transitions are given in the Supporting Information (Figures S3a,c). On the other hand, the intensity of the $(220)_S$ for $Li_{0.33}$NCM in Figure 1b begins to increase at about 300 °C (more details in the Supporting Information, Figures S3b,c); thereafter, it continuously rises up to 560 °C, and falls only slightly from 560 to 600 °C. Since the intensity change of the $(220)_S$ peak is an important indicator for understanding the migration of the cation, and the corresponding structural changes during the thermal decomposition of layer-structured cathode materials, we offer some semi-quantitative analysis here.

As we know, the rhombohedral-, spinel-, and rock-salt structures are all based on a cubic-closed framework packing oxygen atoms, with tetrahedral sites or octahedral sites occupied by cations. In the layered rhombohedral structure (*R-3m* symmetry), lithium- and transition metal-cations occupy alternating octahedral layer sites between the oxygen layers. When the random mixing of cations in each layer completely destroys this alternating sequence, the layered rhombohedral structure changes into the rock-salt structure (*Fm3m* symmetry). In the $LiMn_2O_4$-type spinel structure (*Fd3m* symmetry), lithium cations take the 8a tetrahedral sites while transition metal cations take only the 16d octahedral sites. When both tetrahedral- and octahedral-sites are occupied by the transition-metal atoms, a Co_3O_4 (e.g., M_3O_4)-type spinel is formed. Therefore, there is a close relationship between these types of structures, and the change from one type to another inevitably involves the migration of cations. To correlate the movement of atoms with the intensity variation of diffraction peaks, we may consider the structure factor F_{hkl} because it contains information on the symmetry of the distribution of atoms, and $(F_{hkl})^2$ is proportional to the intensity of diffraction peaks I_{hkl}. Disregarding other contributors to I_{hkl}, such as multiplicity, the Lorentz polarization factor, the temperature factor, and the absorption factor, all of which are independent of the structure, the amplitude squared of the structure factor alone is a good indicator of peak intensity. For the layered rhombohedral structure, if we define f_{oct1} as the average atomic-scattering power at the lithium octahedral sites, f_{oct2} as the average atomic-scattering power at transition-metal octahedral sites, and f_O as the atomic-scattering power of oxygen that builds up the skeleton, then the structural factors for the rhombohedral-$(003)_R$ and $(104)_R$ peaks can be calculated, respectively, as $(3f_{oct1} - 3f_{oct2} - 1.1f_O)$, and $(3f_{oct1} + 3f_{oct2} + 5.8f_O)$. The migration of transition metals from their own layer to the lithium layer greatly increases f_{oct1} due to the much larger atomic-scattering power of the transition metals. Since the f_{oct1} and f_{oct2} have opposite signs for the $(003)_R$ peak, the increased f_{oct1} will reduce significantly the amplitude square of F_{hkl}. In contrast, f_{oct1} and f_{oct2} have the same signs in the structure factor of the $(104)_R$ peak, and therefore, the increase of f_{oct1} will engender an increase in the amplitude square of F_{hkl} for the $(104)_R$ peak. This is the origin of using the intensity ratio of the (003) to (104) peaks to indicate the degree of cation mixing (transition metals in lithium-layer sites). During the initial stage of heating, the reducing intensity ratio of the $(003)_R$ to $(104)_R$ peaks in the TR-XRD patterns clearly denotes the migration of transition metal cations into the lithium layers where vacancies had been created during the overcharge process. For the spinel structure, defining f_{tetra} as the average atomic-scattering power at tetrahedral sites, f_{oct} as the average atomic-scattering power at octahedral sites, and f_O as the atomic-scattering power of oxygen that builds up the skeleton, the structure factors for the peaks of the spinel $(220)_S$ and $(422)_S$ are derived, respectively, as $(-8f_{tetra} - 0.9f_O)$ and $(8f_{tetra} - 0.8f_O)$; there is no contribution from f_{oct} as the symmetry of the octahedral sites cancels it out. When transition metals move from octahedral to tetrahedral sites in a spinel structure, the average atomic-scattering power f_{tetra} is greatly increased. Since f_O is much smaller than f_{tetra} for transition metals, an increase in the latter will directly enhance the absolute value of F_{hkl}, for the $(220)_S$ and $(422)_S$ peaks. In contrast, the structure factors for $(331)_S$ and $(531)_S$ peaks calculated, respectively, as $(5.7f_{tetra} - 8f_{oct} + 6.4f_O)$, and $(5.7f_{tetra} - 8f_{oct} - 3.7f_O)$ will decline when transition metals move from octahedral to tetrahedral sites. Therefore, with such increasing migration, we would expect an enhancing intensity of the $(220)_S$ and $(422)_S$ peaks accompanied with decreasing intensity of the $(331)_S$ and $(531)_S$ peaks; this is what was observed in the TR-XRD patterns of the $Li_{0.33}$NCM depicted in Figure 1b. Therefore, we have obtained confirmation of the steady migration of transition metals from their original octahedral sites to the adjacent tetrahedral sites. More specifically, Co is most likely is responsible for this migration, as we discuss later for findings from X-ray absorption spectroscopy. This continuous migration of Co cations to the tetrahedral sites and formation of a relatively stable Co_3O_4-type spinel structure might be one of the contributors to the higher thermal stability of $Li_{0.33}$NCM cathodes, thereby postponing the more dangerous phase-transition to the rock-salt phase at higher temperatures. Unlike $Li_{0.33}$NCM, $Li_{0.33}$NCA evolved through a different structural route. As can be seen from Figure 1a (and Figure S3a, Supporting Information), the intensities of the $(220)_S$ and $(422)_S$ peaks are weak in the $Li_{0.33}$NCA sample: they first exhibited an increase, reaching a maximum around 313 °C, and then declined and gradually disappeared. This suggests that transition metals initially migrate momentarily to the tetrahedral sites, and then move to the adjacent octahedral sites (likely those octahedral sites occupied by lithium in the original rhombohedral structure)

to form the rock-salt structure. Figure S4 in the Supporting Information illustrates the cations' migration paths from the octahedral to tetrahedral sites and then to the adjacent octahedral sites. Interestingly, if only the former migration of the transition-metal ions was involved, we should see the opposite change of the $(220)_S$ and $(422)_S$ peak intensities compared to those for the $(331)_S$ and $(531)_S$ peaks, as we explained earlier for the $Li_{0.33}$NCM case. However, this co-relationship was not replicated exactly in the TR-XRD patterns for the $Li_{0.33}$NCA sample. Therefore, other factors, such as oxygen release during heating may play an important role in these structural changes, accelerating their thermal decomposition.

3. Combined In Situ TR-XRD and Mass Spectroscopy (MS)

To monitor and analyze gas species released from the overcharged cathode materials during thermal decomposition, and correlate them with the changes in crystal structure, we developed new a technique combining TR-XRD with mass spectroscopy (MS), thereby collecting TR-XRD and MS data simultaneously during heating, as illustrated in Scheme 1b. **Figure 2** shows some preliminary results from the overcharged $Li_{0.33}$NCA cathode. **Figure 3**a,b, respectively, illustrate a series of TR-XRD patterns during heating of the $Li_{0.33}$NCA sample from 25 to 500 °C (at a rate of approximately 2 °C min^{-1}) in the absence of the electrolyte, and the corresponding signals for oxygen gas (O_2) simultaneously detected by MS. The TR-XRD patterns in Figure 2a have similar phase-transition behaviors as observed in Figure 1a for the $Li_{0.33}$NCA sample, apart from some minor differences in the phase-transition temperatures due to kinetic effects caused by the different heating rates used. Here, during heating, we observed two distinct oxygen-release peaks with their centers around 230 and 300 °C in the MS results (Figure 2b). These peaks are clearly correlated with the two structural phase-transitions shown in the TR-XRD patterns in the left panel of Figure 2. The beginning of first noticeable oxygen release observed at about 180 °C is close to the starting temperature of the structural transition from the initial layered structure to the spinel structure, as shown in the TR-XRD results. After the intensity of the first peak reached the maximum at about 230 °C and started decreasing, a second oxygen release peak arose around 250 °C and continued to 500 °C, with its center at about 300 °C. This second peak relates to the phase transition from the disordered spinel structure to the NiO-like rock-salt structure between 250 and 500 °C. More O_2 gas is released during the second phase transition than during the first one, consistent with the following theoretical calculations:

$$Li_{0.33}M(^{3.67+})_{1.0}O_2 \text{ (layered, } R\text{-}3m) \rightarrow Li_{0.33}M(^{3.21+})_{1.0}O_{1.77} \text{ (spinel, } Fd3m) + 0.115O_2\uparrow \quad (1)$$

$$Li_{0.33}M(^{3.21+})_{1.0}O_{1.77} \text{ (spinel, } Fd3m) \rightarrow Li_{0.33}M(^{2.33+})_{1.0}O_{1.33} \text{ (rock-salt, } Fm3m) + 0.22O_2\uparrow \quad (2)$$

Here, M denotes the Ni, Co, and Al ions. The first (Equation 1) is associated with oxygen release resulting from the phase transition from the initial layered structure to the disordered spinel structure. The second (Equation 2), with larger oxygen release, corresponds to the phase transition from the spinel structure to the NiO-type rock-salt structure. These preliminary results, clearly demonstrating the co-relationship between oxygen releases and the crystal structural phase-transitions afford very valuable information for exploring thermal instability and thermal runaway for various cathode materials charged to different states. More systematic studies and further development of this combined TR-XRD and MS technique are underway.

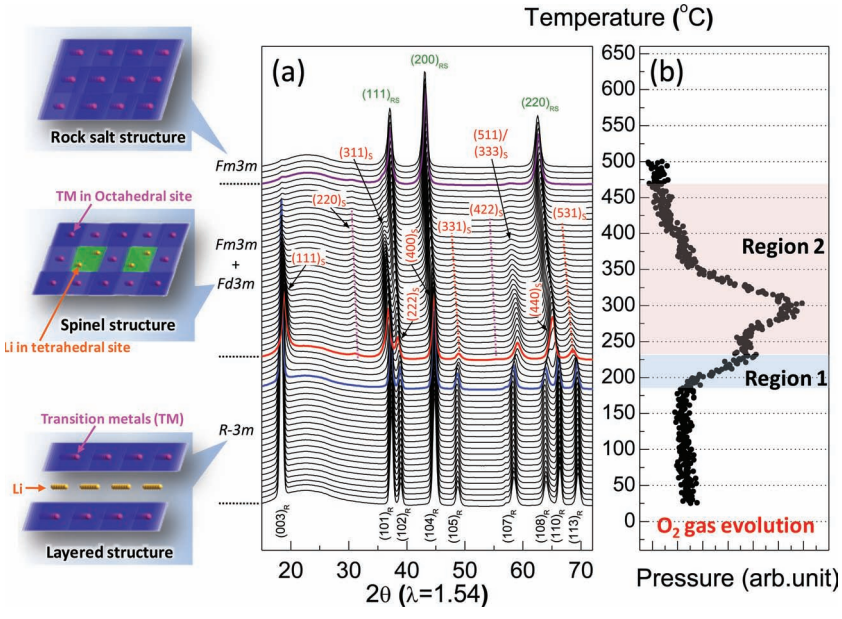

Figure 2. a) Time-resolved (TR) XRD patterns and b) results from simultaneously measured mass spectroscopy (MS) that trace oxygen gas released from the overcharged $Li_{0.33}Ni_{0.8}Co_{0.15}Al_{0.05}O_2$ during heating up to 500 °C. The cathode sample in a glass tube was heated from 25 to 500 °C in 4 h during the TR-XRD and MS measurements (heating rate 2.0 °C min^{-1}). The left panel shows the ideal crystal-structure models for rhombohedral, spinel, and rock-salt structures.

4. In Situ X-Ray Absorption Spectroscopy (XAS)

X-ray absorption spectroscopy (XAS) spectra are divisible into two parts: The XANES (X-ray absorption near edge structure) region covering about 30 eV near the absorption edge and the EXAFS (extended X-ray absorption fine structure) region, which starts at 40 eV above the absorption edge and extends the energy range by several hundred eVs with weak oscillatory wiggles. XANES spectra provide useful information about the average oxidation-states and the site-symmetry changes around the absorbing atoms. On the other hand, the EXAFS spectra give quantitative local structural information, such as bond length, the degree of ordering, and the coordination number around the absorption atoms.

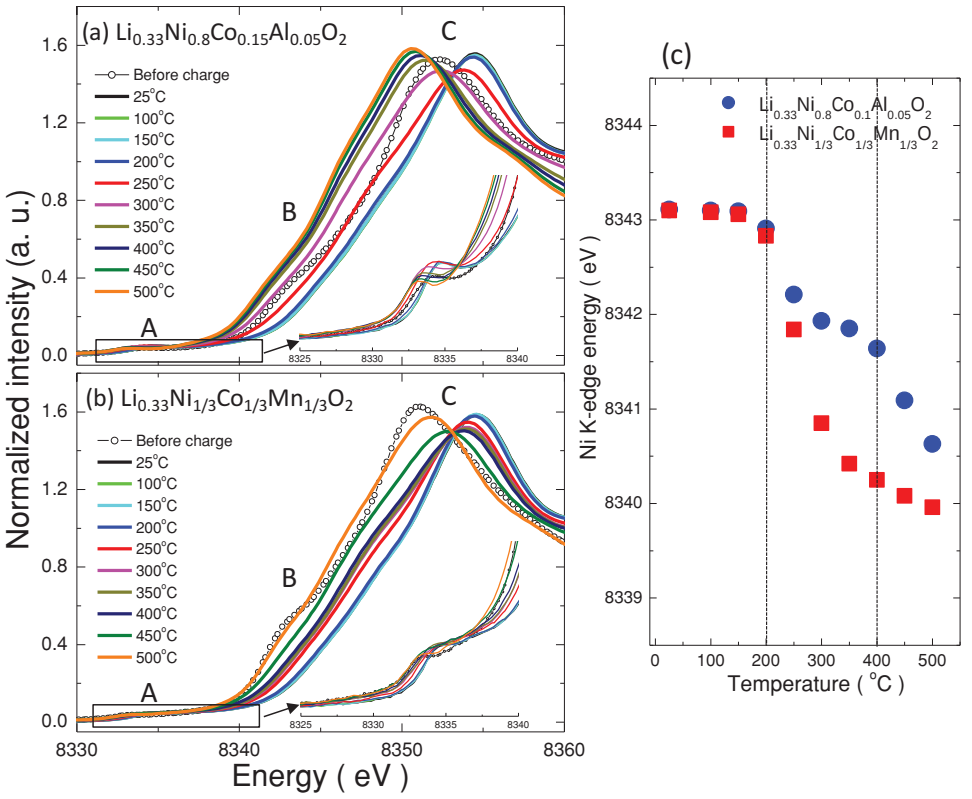

Figure 3. Ni K-edge XANES spectra of the overcharged a) $Li_{0.33}Ni_{0.8}Co_{0.15}Al_{0.05}O_2$ and b) $Li_{0.33}Ni_{1/3}Co_{1/3}Mn_{1/3}O_2$ electrodes during heating up to 500 °C. Insets show the detailed feature of pre-edge region A. c) Variations of the Ni K-edge positions at the first inflection point for both cathodes as a function of heating temperatures.

More detailed theory, analyses, and experimental descriptions of XAS spectroscopy are given in several review papers.[69–72] Whilst TR-XRD can monitor the average changes in crystal structure and phase transitions during thermal decomposition, XAS can probe the local structural changes surrounding the absorbing atoms in an elemental, selective way. Therefore, their combination affords greater insight about how the local structure changes around each transition metal atom, such as Ni, Co, and Mn, in overcharged $Li_xNi_{0.8}Co_{0.15}Al_{0.05}O_2$ and $Li_xNi_{1/3}Co_{1/3}Mn_{1/3}O_2$ cathodes, as well as how they contribute to the phase transitions during thermal decomposition. In this section, we discuss the Ni, Co, and Mn K-edges XANES and EXAFS spectra for overcharged $Li_{0.33}Ni_{0.8}Co_{0.15}Al_{0.05}O_2$ ($Li_{0.33}$NCA) and $Li_{0.33}Ni_{1/3}Co_{1/3}Mn_{1/3}O_2$ ($Li_{0.33}$NCM) cathodes during heating. The XANES- and EXAFS-spectra are both sample- and temperature-dependent; hence, it is difficult to compare the results at different temperatures. Fortunately, the structural changes during heating are irreversible; due to the permanent loss of oxygen, the structure of a sample probed at room temperature after cooling down has remained the same as it was at high temperatures. Therefore, the XAS spectra were acquired at room temperature after heating the samples to different temperatures.

4.1. In Situ X-Ray Absorption Near Edge Structure (XANES)

Figures 3, **4**, and **5**, respectively, illustrate the Ni, Co, and Mn K-edge XANES spectra for charged $Li_{0.33}$NCA and $Li_{0.33}$NCM cathodes during heating up to 500 °C. All spectra reveal three distinct edge features, marked as A, B, and C in the XANES spectra at each K-edge. The weak absorption pre-edge peaks "A", also shown in detail in the inset of each figure, are associated with the dipole-forbidden 1s → 3 delectronic transitions of Ni, Co, and Mn. This transition becomes partially allowed when the 3d and 4p orbital hybridize due to the non-centrosymmetric environment or to structural distortion in local symmetry between the transition metals and oxygen coordination.[73–75] Therefore, the transition metals in tetrahedral sites usually show much more intense pre-edge peaks than do those in the octahedral sites due to a decrease in the inversion center in the tetrahedral-coordination symmetry.[76] The shoulder peak "B" corresponds to the electronic dipole-allowed transition of an 1s core electron to an unoccupied 4p bound state, which is modified by the ligand-to-metal charge transfer (LMCT) effect, or the so-called "shake-down" process.[73,74,77,78] The strong main absorption peak "C" is a dipole-allowed 1s → 4p transition without this "shake-down" process. In general, the shift in edge energy is associated with changes in the average oxidation state of the absorbing atoms being probed. For example, the edge-shift to higher energies indicates increased average oxidation states since the core electrons are bonded more strongly to the nucleus and their photo-ionization necessitates higher photon energies. As seen in Equations (1,2), the average oxidation state of transition metals decreases to compensate for the oxygen released from the overcharged $Li_{0.33}$NCA and $Li_{0.33}$NCM cathodes during thermal decomposition. Therefore, unlike

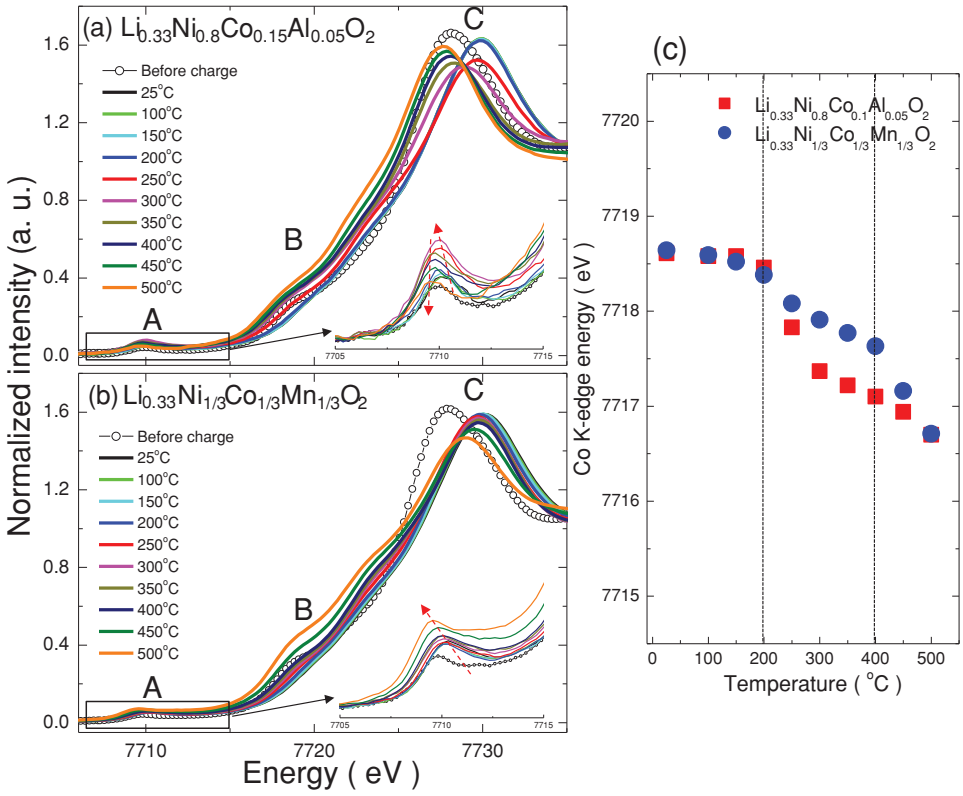

Figure 4. Co K-edge XANES spectra of overcharged a) $Li_{0.33}Ni_{0.8}Co_{0.15}Al_{0.05}O_2$ and b) $Li_{0.33}Ni_{1/3}Co_{1/3}Mn_{1/3}O_2$ electrodes during heating up to 500 °C. Insets show the detailed feature of pre-edge region A. c) Variations of the Co K-edge positions at the first inflection point for both cathodes as a function of heating temperatures.

TR-XRD where the thermal decomposition is identified by the phase transitions, the thermal decomposition can be studied by the reduction of the average oxidation state for each transition metal in an elemental selective way from the in situ XANES spectra at the Ni, Co, and Mn K-edges.

Figure 3a,b show the Ni K-edge XANES spectra for the overcharged $Li_{0.33}$NCA and $Li_{0.33}$NCM cathodes at various heating temperatures. Comparison of the Ni K-edge's position before and after charge (25 °C spectra) for both materials reveals that Ni atoms were oxidized from Ni^{3+} to Ni^{4+} for the $Li_{0.33}$NCA

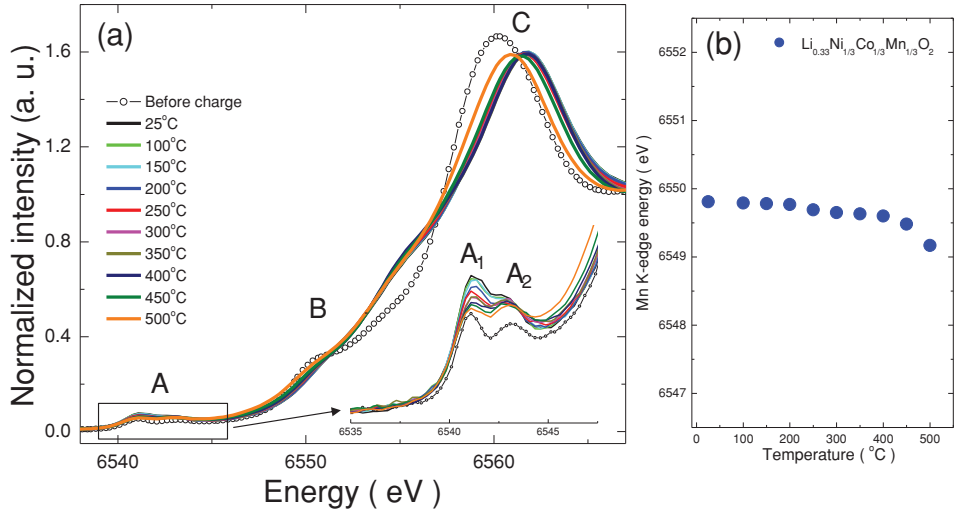

Figure 5. a) Mn K-edge XANES spectra of overcharged $Li_{0.33}Ni_{1/3}Co_{1/3}Mn_{1/3}O_2$ electrodes during heating up to 500 °C. The inset shows detailed feature of pre-edge region A. b) Variations of the Mn K-edge positions at the first inflection point for both cathodes as a function of heating temperature.

sample, and from Ni^{2+} to Ni^{4+} for the $Li_{0.33}$NCM sample, at the overcharged state, during which two-thirds of the lithium was extracted. The equivalent spectra during heating shown in Figure 3a,b exhibit a clear shift of the entire edge towards lower energies, suggesting that thermal decomposition occurs to a large extent at Ni sites in both overcharged cathodes. For both, the edge-shift starts above 200 °C, coincident with the phase transition from a layered- to a LiM_2O_4-type spinel structure depicted in Figure 1a,b, revealing that the migration of Ni into the lithium layer starts first, and is responsible for this initial phase-transition in both overcharged cathodes. However, edge-shifting behaviors in the $Li_{0.33}$NCA and $Li_{0.33}$NCM samples differ at temperatures above 250 °C. While the former sample showed a continuous large edge-shift above 250 °C, and reached close to Ni^{2+} at 400 °C, the latter sample displayed much slower edge-shifts, especially between 250 and 400 °C. Interestingly, this temperature range corresponds to the range of the wide M_3O_4-type spinel structure observed in the TR-XRD for the overcharged $Li_{0.33}$NCM samples (Figure 1b), suggesting the stabilization of spinel phase largely retards the further reduction of Ni and the accompanying oxygen release, so suppressing the phase transition to the rock-salt structure. Another important feature in the XANES spectra is the pre-edge region displayed in the insets of Figure 3a,b. In both cases, the intensity of the weak pre-edge peaks continuously falls with increasing temperatures up to 500 °C. As we described earlier, the intensity pre-edge peak is affected strongly by the site's symmetry and is proportional to the number of Ni cations occupying the tetrahedral sites. The pre-edge peak intensity for both overcharged $Li_{0.33}$NCA and $Li_{0.33}$NCM samples remains weak at all temperatures, implying that most Ni cations stay in the octahedral sites during thermal decomposition in both materials. Accordingly, Ni cations are unlikely to participate in the migration of transition-metal cations into the tetrahedral sites, as indicated by the evolution of the $(220)_S$ and $(442)_S$ peaks with the formation of Co_3O_4-type spinel structure in the TR-XRD patterns during thermal decomposition.

The Co K-edge XANES spectra for the overcharged $Li_{0.33}$NCA and $Li_{0.33}$NCM cathodes in Figure 4a,b also show a similar edge-shift toward lower energies with heating, as observed in the Ni K-edge findings, suggesting that thermal decomposition occurs at Co sites in both overcharged cathodes with rising temperatures. However, we observed several interesting spectral features in the Co K-edge XANES spectra during heating. Those from the $Li_{0.33}$NCA sample show an entire edge-shift during heating up to 500 °C, as evident in the shoulder peak B and main peak C regions in Figure 4a. In contrast, the spectra for the $Li_{0.33}$NCM sample do not show the entire edge-shift but present the evolution of shoulder peak B, while the main peak C shows very little change up to the end of the heating at 500 °C. In addition, the pre-edge peak intensity varied non-monotonically for the $Li_{0.33}$NCA sample, illustrated in the inset of Figure 4a; it first rose with increasing temperatures, attaining a maximum intensity at 350 °C, then declined during further heating to 500 °C. This pattern is different from the continuous decrease in intensity decrease of the Ni K-edge pre-edge peak in the same overcharged $Li_{0.33}$NCA sample (inset of Figure 3a). Co cations in the $Li_{0.33}$NCA sample migrate into the adjacent tetrahedral sites first during the phase transition from the layered to spinel phase, and then quickly move further into the adjacent octahedral sites that originally lay in the Li slab in the layered structure during the phase transition from the spinel- to the final rock-salt-structure (Supporting Information, Figure S4). In contrast, we recorded a monotonic enhancement in the pre-edge peak's intensity with increasing temperature for the $Li_{0.33}$NCM sample, with a distinct rise especially above 400 °C, which is the opposite to the changes discerned in the Ni K-edge pre-edge intensity in the same overcharged $Li_{0.33}$NCM sample (inset of Figure 3b). Comparing the Co K-edge XANES spectra of the $Li_{0.33}$NCM sample with the reference Co_3O_4 spectrum (Supporting Information, Figure S5) strongly suggests that the evolution of shoulder peak B is the typical signature of the formation of the Co_3O_4-type spinel phase. Our findings demonstrated that the Co cations continuously move into the tetrahedral sites and largely remain therein sites until temperatures reach as high as 500 °C. Therefore, the Co_3O_4-type spinel phase is stabilized over much wider temperature ranges (350–500 °C) in the overcharged $Li_{0.33}$NCM sample than in the $Li_{0.33}$NCA sample. These results correspond very well with the findings from TR-XRD.

The Mn K-edge XANES spectra for the overcharged $Li_{0.33}$NCM sample, shown in Figure 5a, differ from the Ni and Co K-edge spectra; the former show little change up to 450 °C, denoting better thermal stability of the Mn sites than others. A doublet of two overlapping peaks "A_1" and "A_2" appearing in the pre-edge peaks shown in the inset is characteristic of manganese 4^+ oxides, and the slight drop in intensity in the A_1 peak during heating could be due to either a slight reduction of Mn^{4+} ions, and to structural modifications, such as variations in the corner- and edge-sharing configurations around the MnO_6 octahedra[79] in the $Li_{0.33}$NCM sample during thermal decomposition. The Mn K-edge XANES results clearly demonstrate the excellent thermal stability of Mn cations.

To compare the changes in the average oxidation states of the Ni, Co, and Mn cations in the overcharged $Li_{0.33}$NCA and $Li_{0.33}$NCM cathodes during thermal decomposition, we plot the variations of the edge positions at the first inflection point in the the Ni, Co, and Mn K-edge XANES spectra, respectively, in Figure 3 c, 4c, and 5b as a function of heating temperature. The Ni K-edge shows the largest edge-shift of around 3.0 eV up to 500 °C compared with the Co K-edge-shift (around 1.8 eV) and that of Mn (around 0.5 eV, largely occurring above 400 °C), highlighting the major thermal instability due to Ni, and the main contribution of Mn to thermal stability. When comparing the Ni edge-shifts between two overcharged cathodes, the larger shift in the Ni K-edge occurs in the $Li_{0.33}$NCA sample from 200 to 350 °C, with a value of about 2.5 eV, which is more than the shift in the $Li_{0.33}$NCM sample at a temperature of 500 °C. This finding clearly demonstrates the much slower thermal decomposition at the Ni sites in the $Li_{0.33}$NCM sample than in the $Li_{0.33}$NCA sample, which we attribute to the more stable Co_3O_4-type spinel phases in the $Li_{0.33}$NCM sample covering a wider temperature range, as is evident from the TR-XRD results in Figure 1. The absolute average oxidation states of Ni in both overcharged cathodes with heating temperatures were estimated by comparing with the edge-shifts of standard materials of Ni ions, such as NiO(Ni^{2+}), $LiNiO_2$(Ni^{3+}), and fully delithiated $Li_{0.0}NiO_2$($^{4+}$), in the Supporting Information (Figure S6). During

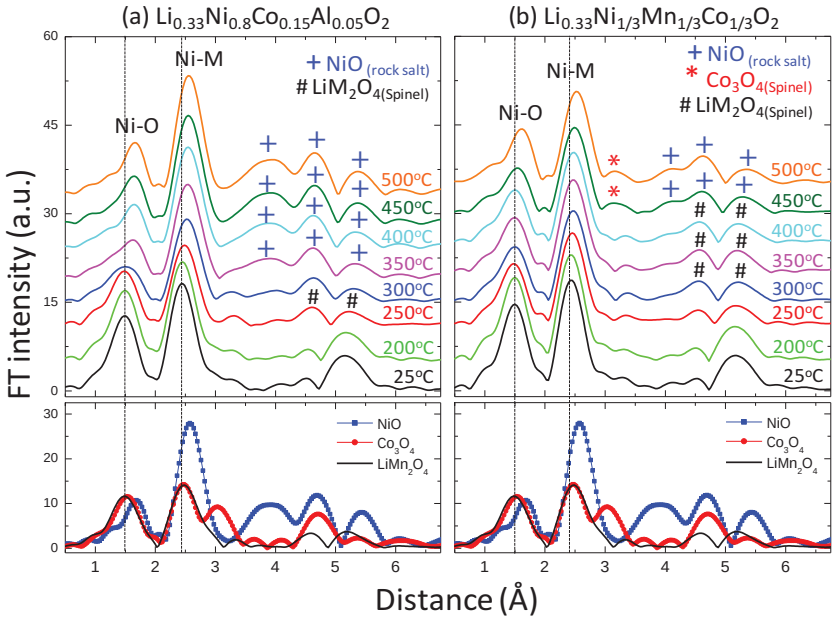

Figure 6. Comparison of the Ni K-edge Fourier transform magnitudes of k^3 weighted EXAFS spectra of the overcharged a) $Li_{0.33}Ni_{0.8}Co_{0.15}Al_{0.05}O_2$ and b) $Li_{0.33}Ni_{1/3}Co_{1/3}Mn_{1/3}O_2$ electrodes with reference oxides spectra (bottom panel) during heating up to 500 °C.

heating from room temperature to 500 °C, the Ni ions in both charged cathodes are estimated as falling from Ni^{4+} to close to Ni^{2+}. Considering the 80% Ni content in $LiNi_{0.8}Co_{0.15}Mn_{0.05}O_2$ versus the 33% in $LiNi_{1/3}Co_{1/3}Mn_{1/3}O_2$, the amount of oxygen released from the $Li_{0.33}$NCA during heating to 500 °C is much more than that from the $Li_{0.33}$NCM sample. The edge-shifts in the Co K-edge spectra also suggest a slower and more gradual thermal decomposition during heating at the Co sites in the $Li_{0.33}$NCM sample than in the $Li_{0.33}$NCA sample.

4.2. Extended X-Ray Absorption Fine Structure (EXAFS) Spectra

To identify the local structural variations around the Ni-, Co-, and Mn-sites in the overcharged $Li_{0.33}$NCA and $Li_{0.33}$NCM cathodes during thermal decomposition, we plotted, in **Figure 6**, **7**, and **8**, respectively, the Fourier-transform (FT) magnitudes of the EXAFS spectra of their k^3-weighted K-edges after heating up to 500 °C. Before heating, at 25 °C, all FT spectra for the overcharged $Li_{0.33}$NCA and $Li_{0.33}$NCM samples exhibit the typical FT features of the layered structure (*R-3m* symmetry), with four distinct FT peaks located at around 1.5, 2.4, 4.4, and 5.2 Å.[73,74,80,81] We note that the actual bond length may be ca. 0.2–0.4 Å and longer because the FT spectra were not phase-corrected. We attribute the strong first and second peaks at approximately 1.5 and 2.4 Å, respectively, to the single scattering paths of the closest oxygen (i.e., M–O) and the second neighboring transition metals within the same *a–b* plane (i.e., M–M) surrounding the absorbing Ni, Co, and Mn atoms. In general, the FT peaks over 4 Å include several multiple-scattering paths as well as single-scattering paths. The FT peaks around 4.4 and 5.2 Å mainly result from combined single M–M and multiple M–M–M scattering within and/or two adjacent transition metal planes.[73,74,80,81]

We monitored the local structural changes and the evolution of new phases surrounding Ni sites in overcharged $Li_{0.33}$NCA and $Li_{0.33}$NCM samples during heating; these are clearly evident in the FTs of the EXAFS spectra in Figure 6a,b. To easily identify the evolution of local phases, we also plotted our reference EXAFS spectra of NiO(rock salt), $LiMn_2O_4$(spinel), and Co_3O_4(spinel), shown in the bottom panels. The spectra for the overcharged $Li_{0.33}$NCA sample shows an initial local structural change around Ni sites at 250 °C, from a layered-to-LiM_2O_4-type spinel structure (marked as "#"), agreeing well with the TR-XRD results in Figure 1a. Above 350 °C, the evolution of the FT peaks associated with the rock-salt phase (marked as "+") were pronounced in the $Li_{0.33}$NCA spectra, with a significant expansion of the bond lengths of Ni–O and Ni–M during heating up to 500 °C. Interestingly, we did not detect FT spectra peaks due to the Co_3O_4-type spinel structure formation around Ni sites in the overcharged $Li_{0.33}$NCA sample for the whole temperature range. On the other hand, the spectra for the overcharged $Li_{0.33}$NCM

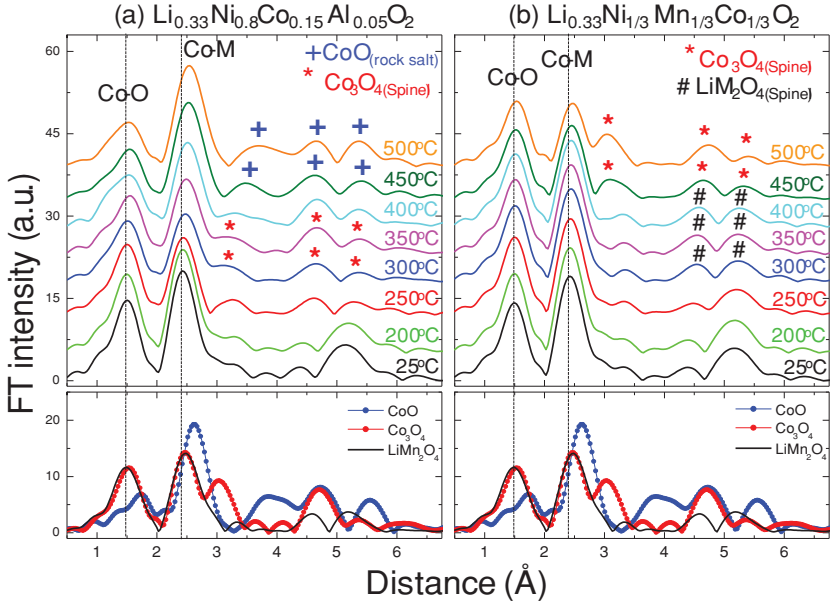

Figure 7. Comparison of the Co K-edge Fourier transform magnitudes of k^3 weighted EXAFS spectra of the overcharged a) $Li_{0.33}Ni_{0.8}Co_{0.15}Al_{0.05}O_2$ and b) $Li_{0.33}Ni_{1/3}Co_{1/3}Mn_{1/3}O_2$ electrodes with reference oxides spectra (bottom panel) during heating up to 500 °C.

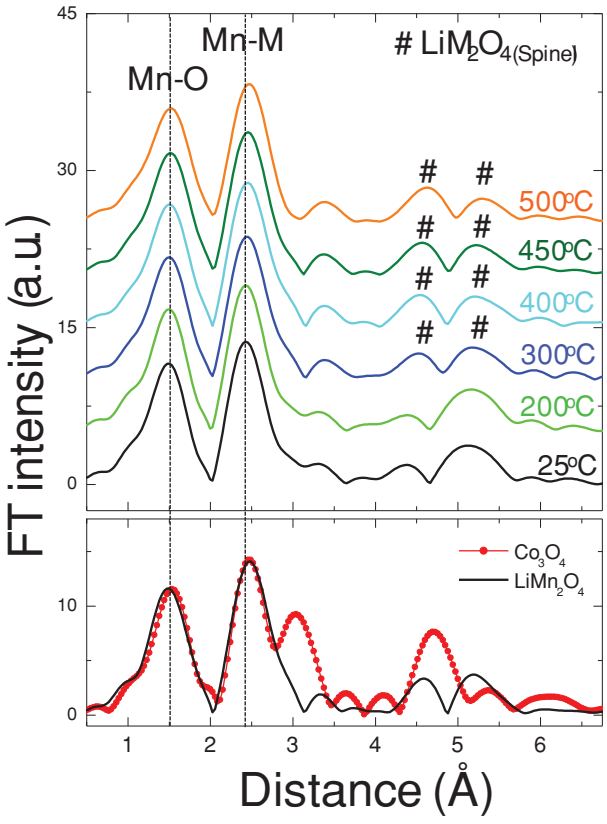

Figure 8. Mn K-edge Fourier transform magnitudes of k^3 weighted EXAFS spectra of the overcharged $Li_{0.33}Ni_{1/3}Co_{1/3}Mn_{1/3}O_2$ electrodes in comparison with reference oxides spectra (bottom panel) during heating up to 500 °C.

sample show much more stable LiM_2O_4-type spinel structure around Ni sites during heating than the $Li_{0.33}$NCA sample. In addition, even after heating to 500 °C, the FT features still have mixed contributions of the major rock-salt-type phase and the minor Co_3O_4-type spinel phase. Although the former phase was not clearly evident in the TR-XRD patterns of the overcharged $Li_{0.33}$NCM sample, even above 500 °C (Figure 1b), the FT spectra features of the $Li_{0.33}$NCM sample heated at 500 °C clearly reveals that already part of the local structure around the Ni sites has transformed into the rock-salt-type phase. This tells us that the XAS technique can provide valuable information about local structural changes that the average technique of TR-XRD cannot do, demonstrating the importance of using a combination of XRD and XAS techniques for this type of study. A comparison of the overall variations in the FT features for the overcharged $Li_{0.33}$NCA and $Li_{0.33}$NCM samples implies that the Ni sites in the $Li_{0.33}$NCM sample are much more thermally stable than those in the $Li_{0.33}$NCA sample, agreeing very well with our Ni K-edge XANES results.

Figure 7 compares the FT magnitudes of Co K-edge EXAFS spectra for the overcharged $Li_{0.33}$NCA and $Li_{0.33}$NCM cathodes during heating with those of the reference oxides. In contrast to the Ni sites, where no phase transformation to the Co_3O_4-type phase occurred during heating to 400 °C, the Co sites in the $Li_{0.33}$NCA sample were transformed to the Co_3O_4-type structure, thus corresponding well with the changes in the pre-edge peak intensity in the Co K-edge XANES spectra. At higher temperatures, we clearly observed in the $Li_{0.33}$NCA spectra the evolution of the FT peaks associated with the rock-salt phase (marked as "+"). However, the higher formation temperatures of the rock-salt-type structure for the Co sites than the Ni sites, as apparent in the Ni and Co K-edges FT spectra (Figure 6a and 7a) demonstrates that the Co sites are more thermally stable than the Ni site in the overcharged $Li_{0.33}$NCA sample. The variations of the FT peaks in the $Li_{0.33}$NCM sample show clear LiM_2O_4-type phase-evolution followed by Co_3O_4-type phase-evolution in the Co sites during heating, i.e., quite different from the evolution of the Co K-edge FT spectra in the $Li_{0.33}$NCA sample. Even at 500 °C, the local structure around Co still remains stabilized with a Co_3O_4-type spinel phase, not with a rock-salt phase, confirming much better thermal stability of the Co sites in the $Li_{0.33}$NCM sample than in the $Li_{0.33}$NCA sample.

Figure 8 shows the variations of FT magnitudes of Mn K-edge EXAFS spectra for the overcharged $Li_{0.33}$NCM cathode. While the FT peaks above approximately 3 Å show small changes in their intensity and shapes close to the $LiMn_2O_4$-type features during heating, the first and second FT spectra peaks within approximately 3 Å range do not change up to 400 °C, revealing excellent thermal stability of the MnO_6 framework in the overcharged $Li_{0.33}$NCM sample. The findings from the Mn K-edge XANES and EXAFS during heating clearly highlight the critical role of Mn cations in supporting the thermal stability of $LiNi_{1/3}Co_{1/3}Mn_{1/3}O_2$-type cathode materials by sustaining the MnO_6 framework. The Ni, Co, and Mn K-edge XANES and EXAFS spectra of the overcharged $Li_{0.33}$NCM sample interestingly indicate the possible transition-metal clustering and structural preference of each element. Seemingly, Ni sites prefer to form the rock-salt-type structures, Co sites preferentially form the Co_3O_4-type spinel, while the Mn sites favor forming the $LiMn_2O_4$-type spinel structure. These structures co-exist at 500 °C, with the average structural features close to the Co_3O_4 type spinel-structure.

5. In Situ Transmission Electron Microscopy (TEM)

For the TEM studies, we chose deeply overcharged samples of $Li_{0.15}Ni_{0.8}Co_{0.15}Al_{0.05}O_2$ ($Li_{0.15}$NCA) and $Li_{0.15}Ni_{1/3}Co_{1/3}Mn_{1/3}O_2$ ($Li_{0.15}$NCM) to explore the structural changes initiated by the overcharge process before and after heating.

5.1. Overcharged $Li_{0.15}Ni_{0.8}Co_{0.15}Al_{0.05}O_2$ Particles

Overall TEM observations (**Figure 9**a) for the overcharged $Li_{0.15}$NCA sample show that the particle sizes range from several hundreds of nanometers to a couple of microns. Analyses of selected-area electron-diffraction patterns (SAEDP) indicates that most particles are rhombohedral structures. Figure 9b shows a typical SAEDP from a particle with a selected area of about 240 nm diameter. The pattern has a pseudo-hexagonal one; it can only be indexed as the $[\text{-}1\text{-}21]_R$ diffraction pattern

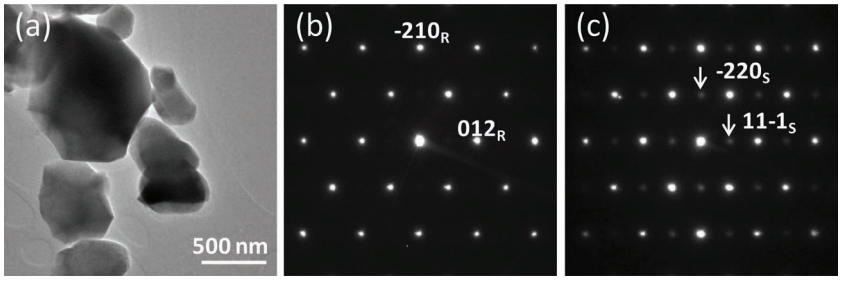

Figure 9. a) Typical morphology of an overcharged $Li_{0.15}Ni_{0.8}Co_{0.15}Al_{0.05}O_2$ particle. b) $[-1-21]_R$ selected-area electron-diffraction pattern (SAEDP) from a particle with a 240 nm diameter selected area. c) SAEDP from the edge of a particle with the selected area of about 120 nm diameter. The arrows show the weak spots of the spinel structure. Subscripts R and S represent rhombohedral and spinel structures, respectively.

of the rhombohedral (the subscript R denotes rhombohedral) structure. This result conforms well to our TR-XRD results for the same sample before heating, showing that, when averaged over a 240 nm diameter area in the SAEDP, the structural information obtained is the same as that in XRD averaging 1 mm^2 sample area (the area of the X-ray beam). However, when we selected a smaller area aperture (approximately 120 nm in diameter) and selected the edge of the particle, we noted diffraction spots of the spinel structure, as shown in Figure 9c. To locate this spinel phase, we collected high-resolution TEM (HRTEM) images. Carefully examining **Figure 10**a, the HRTEM image taken from the edge of an overcharged particle, reveals three different types of areas – rock-salt (RS), spinel (S), and rhombohedral (R) – located from the edge to the core as marked. The RS area has a rectangular pattern, consistent with the arrangement of cations in the $[112]_{RS}$ projection of the rock-salt structure, affording us clear evidence of the presence of this structure at the edge or the surface of the overcharged particle even at room temperature. The pattern of the S area is similar to that of area RS, but exhibits alternating weak and strong contrasts along the $[11-1]_S$ direction, indicating the spinel structure herein, since only this structure has different atomic densities in the $(11-1)_S$ cation planes that engender such weak and strong contrast. The area R has a pseudo-hexagonal pattern, resembling the arrangement of the cations in the $[-1-21]_R$ projection of the rhombohedral structure (see Wu et al.[65] for more details of the cation arrangements in different structures), indicating a rhombohedral structure. Figure 10b shows an HRTEM image taken from another overcharged particle viewed along the $[001]_R$ direction. It clearly exhibits a rock-salt structure at the edge and spinel structure in the area slightly off the edge. Based on these data, we conclude that the particle consists of three phases: rhombohedral, spinel, and rock-salt. The rhombohedral phase is the dominating structure, located in the core of the particle, while the rock-salt structure generally is distributed on the surface. The spinel phase mainly accounts for the shell (slightly off the surface) with a small amount of rhombohedral phase. Therefore, we can categorize the overcharged particle by a core–shell-surface structure with rhombohedral in the core, spinel in the shell, and rock-salt structure on the surface.[65]

After examining many overcharged $Li_{0.15}$NCA particles, we found that most particles have this kind of core–shell-surface structure. The rock-salt surface layer is about a few nanometers thick, while the spinel shell (mixed with small amount of rhombohedral phase) ranges from a few to tens of nanometers. Based on HRTEM and electron diffraction, the relationship between RS and R is determined as:

$$(012)_R \parallel (11-1)_{RS},\ (-210)_R \parallel (-110)_{RS},\ [-1-21]_R \parallel [112]_S$$

At an equilibrium state, the lattice spacing of the $(11-1)_{RS}$ should be larger than that of the $(012)_R$ or the $(22-2)_S$ based on the lattice parameters of the bulk rock-salt structure. However, the HRTEM images (Figure 10a) show that the lattice spacing of the $(11-1)_{RS}$ is basically the same as that of $(012)_R$, indicating that, at room temperature, the lattice parameter of the rock-salt structure on the surface is not relaxed to the equilibrium value, but locked at the smaller value of the mother phase (spinel or rhombohedral phases) in a strain-matched state, where the surface layer is less than the critical thickness and the surface structure is not fully relaxed to the equilibrium state. Such a core–shell-surface structure is difficult to be detected by XRD, which is an averaging technique with much poor spatial resolution than TEM.

We monitored the local structural evolution of the overcharged $Li_{0.15}$NCA particles during heating in.situ. We found that the phase transitions during heating are irreversible, due to the permanent loss of oxygen in high vacuum TEM, as we confirmed by our TR-XRD-combined MS result (Figure 2): the structure of the sample remained the same after cooling down to room temperature as they were at high temperatures. Therefore, the images we acquired at room temperature after heating to different high temperatures are truly representative of

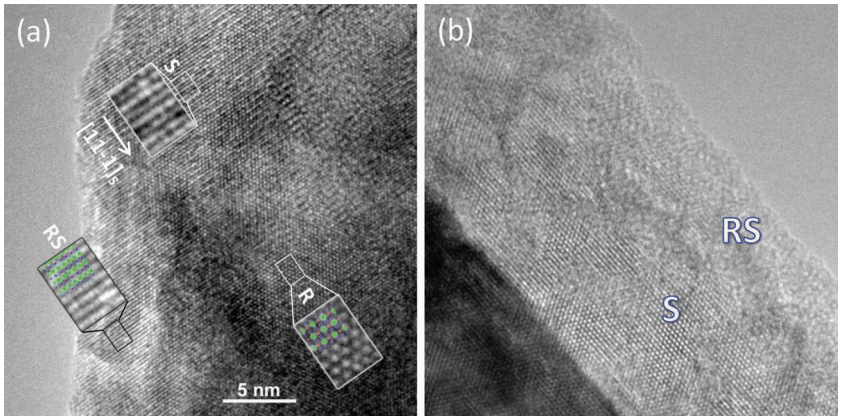

Figure 10. HRTEM images viewed along a) $[-1-21]_R$ and b) $[001]_R$ directions for an overcharged $Li_{0.15}Ni_{0.8}Co_{0.15}Al_{0.05}O_2$ particle. The insets in (a) show the magnified images from the small rectangle areas, indicating the rock-salt (RS), spinel (S), andrhombohedral(R) structures. In (b), although both the spinel and rock-salt structures have hexagonal pattern, the periodicity of the former is twice as that of the latter.

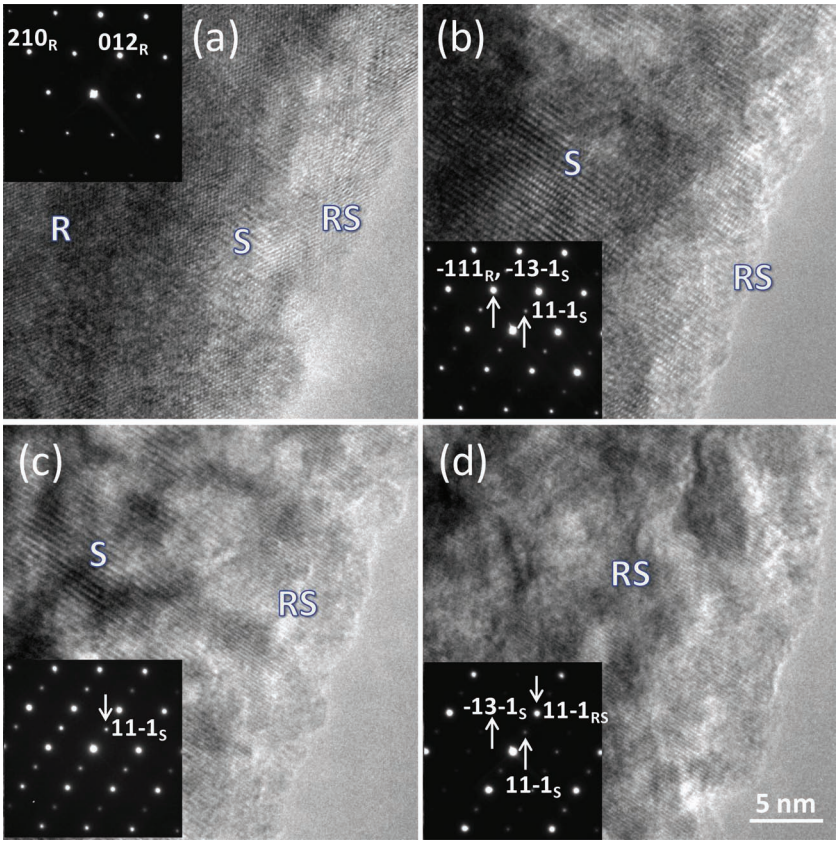

Figure 11. HRTEM images taken from an overcharged $Li_{0.15}Ni_{0.8}Co_{0.15}Al_{0.05}O_2$ particle: a) beforeheating,andafter heating at: b)100, c)200, and d) 300 °C. The insets are the corresponding SAEDPs taken from a large area (approximately 240 nm in diameter) of the same particle.

the sample at high temperatures. **Figure 11**a shows an HRTEM image of an overcharged particle with the beam along the $[\text{-}1\text{-}21]_R$ direction. Although small amounts of rock-salt and spinel phases are apparent in the edge, most of the area constitutes the rhombohedral phase. The SAEDP (inset in Figure 11a) confirms this, as it shows only the spots of the rhombohedral structure. After heating to 100 °C (Figure 11b), the spinel structure, with its alternating strong and weak $(11\text{-}1)_S$ lattice contrast, dominates the edge area. The corresponding SAEDP (inset in Figure 11b) shows weak $11\text{-}1_S$ and $\text{-}1\text{-}11_S$ spots, indicating an increased amount of the spinel phase. After heating to 200 °C (Figure 11c), the intensity of the $11\text{-}1_S$ spot in SAEDP had risen, signifying the overall growth of the spinel phase in the particle. In the edge, however, the spinel phase transformed into the rock-salt phase, which has fine $(11\text{-}1)_{RS}$ fringes. By 300 °C (Figure 11d), the rock-salt phase dominates the particle, though very weak spinel spots remain in the corresponding SAEDP. At 400 °C, the particle transformed completely to the rock-salt phase. Many particles were checked using SAED and HRTEM; we confirmed statistically the majority existence of the rock-salt phase after heating to 400 °C.

5.2. Overcharged $Li_{0.15}Ni_{1/3}Co_{1/3}Mn_{1/3}O_2$ Particles

The sizes of the $Li_{0.15}$NCM particles range from hundreds of nanometer to a few microns, similar to those of the $Li_{0.15}$NCA particles. However, unlike the overcharged $Li_{0.15}$NCA particles, there is no trace whatsoever of the rock-salt structure on the surface. For most particles of the overcharged $Li_{0.15}$NCM, when we tilted the particles to the $[001]_R$ orientation, we observed some reflections that the rhombohedral lattice prohibits. **Figure 12**a shows the SAEDP of the particle. We indexed the spots with strong intensity by the rhombohedral structure. One set of the weak spots marked by the green circles is indexed as the $[111]_S$ pattern of the spinel structure LiM_2O_4 ($M = Ni_{1/3}Co_{1/3}Mn_{1/3}$). Another set of weak spots, marked by the red circles, represents the extinct reflections of the rhombohedral structure, $LiMO_2$, implying a primitive hexagonal structure. We considered the possible cause of the weak spots as being due to Li ion and vacancy ordering, but ruled this out since our calculations of the diffraction intensity show that the intensity of these as-considered superlattice spots due to these two factors would be much weaker than that of the spots we observed. By tilting the sample to the other orientations, we determined that this set of the spots correspond to the CdI_2-type structure MO_2 (denoted as O1) formed by the sliding of two thirds of the MO_2 layers after the removal of the Li from the rhombohedral phase.[66,67] This interpretation is consistent with the TR-XRD observation showing weak O1 peaks in Figure 1b. Figure 12b illustrates the dark-field image formed by applying a small aperture to allow only the 100_{O1} reflection to pass through it. Undoubtedly, the O1 phase (bright area) is distributed at the surface of the particle. The dark-field image (Figure 12c) formed by using the $2\text{-}20_S$ reflection demonstrates that the distribution of the spinel phase is just slightly below the surface. Figure 12d is an HRTEM image from the edge of the particle. The diffractogram (top inset) from the surface (orange circle) shows only the reflections of the O1 phase, while that from the area circled by a blue line (bottom inset) contains the reflections of both the O1 and the spinel phases. Based on these observations, we conclude that most of the overcharged $Li_{0.15}$NCM particles before heating have a core–shell-surface structure with the O1 on the surface, the spinel phase in the shell, and the rhombohedral phase in the core. In comparison with the overcharged $Li_{0.15}$NCA at room temperature, the overcharged $Li_{0.15}$NCM forms an CdI_2-type MO_2 structure at the surface suppressing the oxygen-releasing phase transition to the rock-salt structure. Dark-field images using the reflections of $(100)_{O1}$ and $(2\text{-}20)_S$, respectively, are shown in Figure 12b,c. The dashed lines indicate the same location in Figure 12b,c, and clearly, the distribution of O1 mainly is at the surface, and distribution of spinel slightly off the surface. Figure 12d shows an HRTEM image taken from the edge of the particle. The insets at the top and the bottom are, respectively, the diffractograms from the areas circled in orange and blue, showing the O1

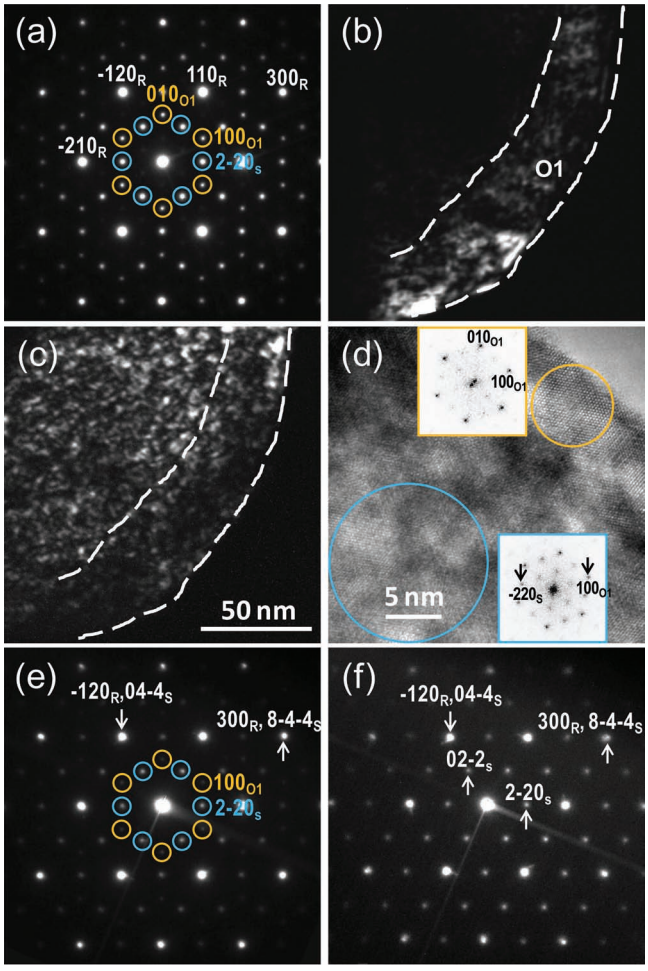

Figure 12. a) SAEDP of an overcharged $Li_{0.15}Ni_{1/3}Co_{1/3}Mn_{1/3}O_2$ particle. b,c) Dark field images using reflections of 100_{O1} (b) and $2\text{-}20_S$ (c). The dashed lines indicate the same location in (b) and (c). d) HRTEM image from the edge of the particle. The insets at the top (orange square) and the bottom (blue square) are the diffractograms from the orange and blue circled areas, respectively. e,f) SAEDP taken from the sample heated at 100 and 300 °C, respectively.

structure at the surface, and a mixture of O1 and spinel slightly off the surface. Figure 12e,f show the SAEDPs after heating to 100 and 300 °C, respectively. The spots of the O1 phase are weakened, whilst those of the spinel phase are strengthened after heating to 100 °C, indicating the transformation of the O1 phase to the spinel phase. Since there is very little Li in the O1 phase, it is much easier for the transition metal to migrate to the tetrahedral sites and form Co_3O_4-type spinel structure with its high intensity of (2-20) spots. After heating at 300 °C, the O1 phase disappears, as shown in Figure 12f where the spots of the O1 phase disappear. These results agree very well with our in situ TR-XRD and XAS results, showing the formation of O1 structure for the overcharged $Li_{0.15}$NCM, rather than the rock-salt structure for the overcharged $Li_{0.15}$NCA at the surface during the overcharge process, helped the formation of Co_3O_4-type spinel in the $Li_{0.15}$NCM during heating. The formation of the Co_3O_4-type spinel in the overcharged $Li_{0.15}$NCM further stabilized the structure, postponing the bulk-phase transition to higher temperatures for the Li_xNCM materials.

6. Conclusions

We employed synchrotron-based time-resolved (TR) XRD and in situ mass spectroscopy (MS) combined with in situ X-ray absorption spectroscopy (XAS) to study the structural changes during heating of $Li_xNi_{0.8}Co_{0.15}Al_{0.05}O_2$ and $Li_xNi_{1/3}Co_{1/3}Mn_{1/3}O_2$ cathode materials overcharged to the $x = 0.33$ level. In addition, the same samples with deeper overcharge states with the $x = 0.15$ level were studied using in situ TEM during heating. The TR-XRD results show clearly different phase-transition behaviors in these two materials. In the overcharged state with $x = 0.33$ level at room temperature, we observed only the rhombohedral structure in the $Li_{0.33}$NCA sample, while in the $Li_{0.33}$NCM sample, a new O1 phase with a CdI_2-type structure appeared in addition to the dominant rhombohedral phase. During heating to 600 °C, the $Li_{0.33}$NCM sample showed much higher phase-transition temperatures from the rhombohedral to the $LiMn_2O_4$-type-spinel structure than did the $Li_{0.33}$NCA sample, with a new phase transition from this $LiMn_2O_4$-type spinel to the Co_3O_4-type spinel structure when heated above 400 °C for the $Li_{0.33}$NCM sample. The structure of the $Li_{0.33}$NCA sample had completely transformed to the rock-salt type at approximately 460 °C; in contrast, the $Li_{0.33}$NCM sample largely retained its Co_3O_4-type spinel structure up to 600 °C due to the increased partial occupancy at the tetrahedral sites of the transition metals (mostly Co). The formation of this Co_3O_4-type spinel structure in the Li_xNCM samples pushes the phase transition to rock-salt structure at a higher temperature, and improves thermal stability. The preliminary results of using the newly developed combined TR-XRD and MS technique show the clear release of oxygen from the overcharged $Li_{0.33}$NCA sample accompanying each phase transition occurring during thermal decomposition.

Although the TR-XRD provides very good road maps of the paths of phase-transition of these two materials, no information is obtainable about the changes in the oxidation state of each transition metal (Ni, Co, and Mn) and their contribution to the thermal stability of these two types of materials. On the other hand, in situ XAS can provide this missing information during thermal decomposition. The XANES results during heating show that, Ni is the most unstable element with the largest and fastest reduction from Ni^{4+} to Ni^{2+}; the reduction of Co is less and slower than that of Ni; and, Mn is the most thermally stable element and remains close to the Mn^{4+} state up to a temperature of 400 °C. The in situ EXAFS results during heating show that Ni cations prefer to form a rock-salt type structure by migrating to the octahedral vacancy sites left by the electrochemically extracted Li cations; Co cations are likely to move to the tetrahedral sites in Co_3O_4-type spinel structure; and, Mn cations are stable, staying at their original octahedral sites. This is the first systematic in situ study with elemental-selective information on the structural changes of these cathode materials with overcharged states during heating. However, just like the in situ TR-XRD, the in situ XAS also is a bulk-averaging technique, probing a sample sized in the millimeter

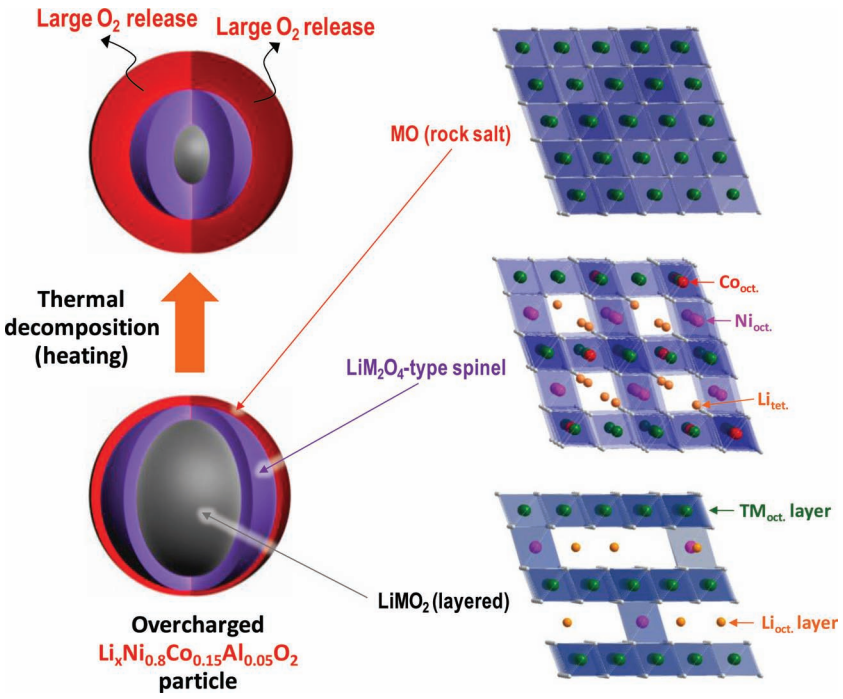

Figure 13. Schematic of the mechanism of thermal decomposition of the overcharged $Li_xNi_{0.8}Co_{0.15}Al_{0.05}O_2$ cathode during heating. The left side shows phase propagation from the surface to core for the overcharged particle. The right side shows the changes in crystal structure and cation distribution.

range. In situ TEM during heating, on the other hand, provides valuable information with location specificity and high spatial-resolution on the structural changes in these two materials. For the deeply overcharged $Li_{0.15}$NCA sample, both spinel and rock-salt phases, which were only observed at high temperatures in the TR-XRD results, are noted at room temperature, located at or near the surface of the samples' particles, in addition to the rhombohedral phase in the core. These spinel- and rock-salt-structural domains, nucleated during overcharge, serve as seeds for the phase transition to the spinel and rock-salt phases, accelerating the thermal decomposition of the $Li_{0.15}$NCA sample during heating. In contrast, in the $Li_{0.15}$NCM sample at room temperature, we observed the O1 type structure at the surface of the sample's particles, in addition to the spinel phase near surface, and rhombohedral phase in the core. During heating, the O1 phase was transformed into the Co_3O_4-type spinel, due to the material's Co content, and thereafter stayed mainly in the Co_3O_4-type-spinel phase at temperatures as high as 300 °C, due to the stabilization effects of the Mn cations, with only a very small portion being transformed to the rock-salt structure.

The scheme in **Figure 13** illustrates the different phase-distributions for the $Li_{0.15}$NCA sample at room temperature obtained by TEM observations, and its phase transition path during heating observed by X-ray techniques. The left panel of Figure 13 depicts the surface as the rock-salt phase and the near-surface as spinel phase at room temperature. During heating, the surface structures propagate towards to the core, and the rock-salt phase becomes the dominant structure at high temperature. The right panel shows the structural model at the atomic level, illustrating the migration of Ni cations to the original Li sites and forming the rock-salt structure during heating.

The structural changes of the $Li_{0.15}$NCM sample are illustrated in **Figure 14**. The left panel of Figure 14 sketches the O1 structure at the surface of the $Li_{0.15}$NCM sample at room temperature. During heating, this phase transforms into the Co_3O_4-type-spinel structure and stays as such to high temperature. The right panel illustrates migration of Co cations to the tetrahedral sites and the unchanged Mn at original octahedral sites. These results suggest that Mn plays a major role in suppressing the formation of the rock-salt structure on the surface, and the combined effects of Mn and Co help to form and maintain the Co_3O_4-type spinel and suppress the transformation to the rock-salt structure during heating. Therefore, increasing the Mn content on the surface

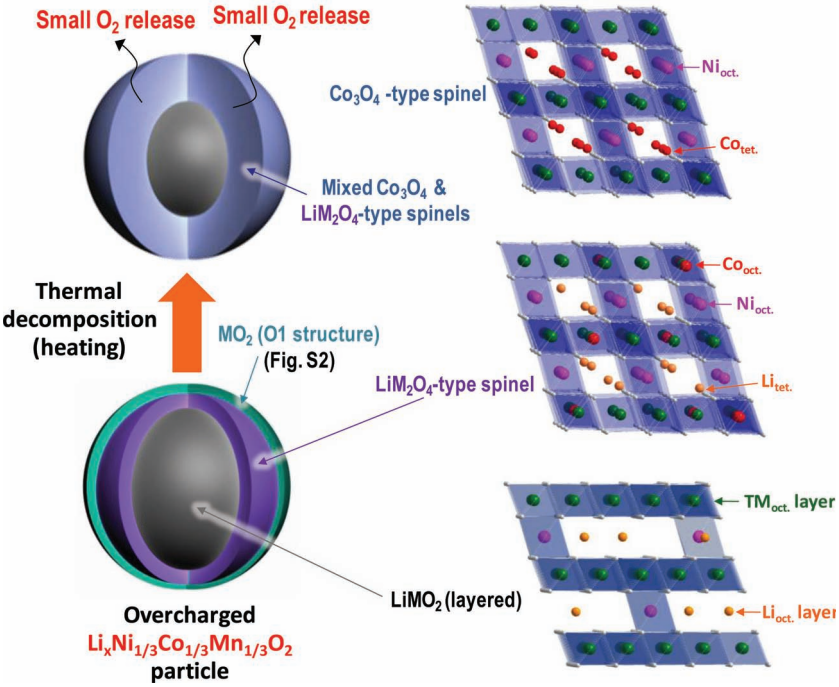

Figure 14. Schematic of mechanism of thermal decomposition of the overcharged $Li_xNi_{1/3}Co_{1/3}Mn_{1/3}O_2$ cathode during heating. The left side shows phase propagation from surface to core for the overcharged particle. The right side shows the changes in crystal structure and cation distribution.

of the particles could effectively improve the thermal stability of the layered cathodes, while retaining the high-energy density by keeping high Ni concentration in the bulk.

7. Experimental Section

Cathode Electrode Fabrication and Electrochemical Test: The cathode materials of $LiNi_{0.8}Co_{0.15}Al_{0.05}O_2$ and $LiNi_{1/3}Co_{1/3}Mn_{1/3}O_2$ were provided by Seimi (Japan) and Fuji Chemical (Japan), respectively. The cathode electrodes were fabricated by slurry casting of 84% of active materials, 8% of carbon black (Chevron), and 8% of PVDF (Kureha) on to Al foil. 2032-type coin cells were assembled using a Li foil anode, a separator (Celgard), and an electrolyte composed of 1.2 M $LiPF_6$ in 3:7 EC (ethyl carbonate)/DMC (dimethyl carbonate). The coin cell was charged at a *C*/18 rate to a level corresponding to a composition of $Li_{0.33}Ni_{0.8}Co_{0.15}Al_{0.05}O_2$ and $Li_{0.33}Ni_{1/3}Co_{1/3}Mn_{1/3}O_2$, estimated from the charge and mass of the active material, by assuming that all the current passed through it was used to extract lithium. The samples for TEM studies were prepared in the same way but more deeply overcharged to a lower Li content as $Li_{0.15}Ni_{0.8}Co_{0.15}Al_{0.05}O_2$ and $Li_{0.15}Ni_{1/3}Co_{1/3}Mn_{1/3}O_2$.

In Situ Time-Resolved XRD and Mass Spectroscopy (MS): The charged cells were transferred to a glove box for disassembly. The charged cathodes were washed in DMC solvent in the glove box and the fine cathode powders (including the binder and conductive carbon) were obtained by scratching away the electrode from the current collector. They were loaded into 0.5 mm diameter quartz capillaries in the glove box and the capillary tip was sealed temporarily with vacuum grease in the glove box. The capillary then was transfer from the glove box and hermetically sealed using an oxygen torch before being mounted on the thermal stage of beamline X7B, at National Synchrotron Light Source (NSLS), Brookhaven National Laboratory (BNL).[53,82,83] The wavelength used at the X7B was 0.3184 Å. To track the structural changes during thermal degradation, XRD spectra continuously were recorded as a set of circles on a two-dimensional image plate detector in the transmission mode during heating from room temperature to 600 °C for 4 h (i.e., heating rate = 2.4 °C min^{-1}). The total recording time for one spectrum was approximately 2.6 min. For the combined TR-XRD and MS experiment, we used unsealed 0.9 mm diameter glass-tube capillaries. One end of the capillary was connected to an inlet with the He carrier gas, and the other end was connected to the mass spectrometer (i.e., residual gas analyzer, RGA) with a flowmeter to detect the gas species released from the powder sample during heating. To prevent the movement of the sample's position caused by the flow of He carrier-gas flow, quartz wools were placed on each side of the powder. The TR-XRD patterns and MS signals simultaneously were collected continuously whilst heating the sample from room temperature to 500 °C for 4 h (i.e., heating rate = 2.0 °C min^{-1}). For making easy comparisons with the results in the literature, we converted all the 2θ angles in this paper to the values corresponding to Cu Kα1 radiation ($\lambda = 1.54$ Å).

In Situ X-Ray Absorption Spectroscopy: Mn, Co, and Ni K-edge XAS spectra were collected at the X18A and X19A Beamlines of the National Synchrotron Light Source (NSLS) using a Si(111) double-crystal monochromator in the transmission mode. The beam intensity was reduced by 30%–40% to minimize the high-order harmonics. The reference spectra of Mn-, Co-, and Ni-metallic foils were collected simultaneously with the sample spectra for the energy calibration.A special sample holder with a heating element and a thermocouple temperature- sensor were used for the in situ high-temperature XAS experiments. The XAS spectra were collected at room temperature after heating the overcharged cathode sample to different high temperatures. The overcharged cathode samples, kept on the Al current collector, were washed by DMC solvent first and then mounted on the sample holder and heated under He-gas protection. The reason of collecting XAS data at room temperature is to obtain a better comparison of the EXAFS results at different heating temperatures because temperature greatly affects the EXAFS spectra. The XANES and EXAFS spectra were processed using the Athena software package.[84] The AUTOBK code was used to normalize the absorption coefficient, and separate the EXAFS signal, $\chi(k)$, from the isolated atom-absorption background. The extracted EXAFS signal, $\chi(k)$, was weighted by k^3 to emphasize the high-energy oscillations and then Fourier-transformed in a k range from 3.0 to 11.5 $Å^{-1}$ for the Mn and Co K-edges and 3.0 to 12.0 $Å^{-1}$ for the Ni K-edge using a Hanning window with a window sill (Δk) of 1.0 $Å^{-1}$, thereby obtaining magnitude plots of the EXAFS spectra in *R*-space (Å).

In Situ TEM: The overcharged cathode particles scraped from the current collector were loaded into a small glass bottle filled with small volume of acetone to disperse them. Their good dispersal was ensured via supersonic vibration before dropping the sample on a TEM carbon-grid. High-resolution transmission electron microscopy (HRTEM) and electron diffraction were carried out using the JEM-3000F microscope operated at 300 kV. The microscope was equipped with an ultra-high-resolution objective-lens pole-piece, and a Gatan double-tilt heating stage that measures temperature to 1 °C accuracy. The vacuum at sample area was about 3×10^{-5} Pa. It was found that the overcharged sample was stable in the high-vacuum environment in TEM. A low beam current and short exposure time were used for recording images to ensure fewer structural changes were induced by the electron beam. The HRTEM images were simulated using computer codes based on the multislice method.

Supporting Information

Supporting Information is available from the Wiley Online Library or from the author.

Acknowledgements

The work was supported by the US Department of Energy, Assistant Secretary for Energy Efficiency and Renewable Energy, Office of Vehicle Technologies; and Office of Science, Office of Basic Energy Science (TEM studies by Lijun Wu and Yimei Zhu) under Contract Number DEAC02-98CH10886. Use of the National Synchrotron Light Source, Brookhaven National Laboratory, was supported by the US Department of Energy, Office of Science, Office of Basic Energy Sciences, under Contract No. DE-AC02-98CH10886. The work at Korea Institute of Science and Technology was supported by Global Research Lab. Program through the National Research Foundation of Korea (NRF) funded by the Ministry of Education, Science and Technology (MEST) (grant number: 2011-00115). The authors acknowledge technical support from the NSLS's beamline scientists at X7B, X18A, and X19A, Drs. Steve Ehrlich, Jonathan Hanson, Syed Khalid, Rei Si, Qi Wang, and Nebojsa Marinkovic.

Received: March 13, 2012
Published online: June 19, 2012

[1] J. M. Tarascon, M. Armand, *Nature* **2001**, *414*, 359.
[2] J. B. Goodenough, Y. Kim, *Chem. Mater.* **2010**, *22*, 587.
[3] B. Scrosati, J. Garche, *J. Power Sources* **2010**, *195*, 2419.
[4] M. Morcrette, Y. Chabre, G. Vaughan, G. Amatucci, J. B. Leriche, S. Patoux, C. Masquelier, J. M. Tarascon, *Electrochim. Acta* **2002**, *47*, 3137.
[5] X. Q. Yang, J. McBreen, W. S. Yoon, C. P. Grey, *Electrochem. Commun.* **2002**, *4*, 649.
[6] M. Holzapfel, P. Strobel, C. Darie, J. Wright, M. Morcrette, E. Chappel, M. Anne, *J. Mater. Chem.* **2004**, *14*, 94.
[7] J. Breger, N. Dupre, P. J. Chupas, P. L. Lee, T. Proffen, J. B. Parise, C. P. Grey, *J. Am. Chem. Soc.* **2005**, *127*, 7529.
[8] J. B. Leriche, S. Hamelet, J. Shu, M. Morcrette, C. Masquelier, G. Ouvrard, M. Zerrouki, P. Soudan, S. Belin, E. Elkaim, F. Baudelet, *J. Electrochem. Soc.* **2010**, *157*, A606.

[9] X. J. Wang, H. Y. Chen, X. Q. Yu, L. J. Wu, K. W. Nam, J. M. Bai, H. Li, X. J. Huang, X. Q. Yang, *Chem. Commun.* **2011**, *47*, 7170.
[10] D. Choi, J. Xiao, Y. J. Choi, J. S. Hardy, M. Vijayakumar, M. S. Bhuvaneswari, J. Liu, W. Xu, W. Wang, Z. G. Yang, G. L. Graff, J. G. Zhang, *Energy Environ. Sci.* **2011**, *4*, 4560.
[11] J. F. M. Oudenhoven, F. Labohm, M. Mulder, R. A. H. Niessen, F. M. Mulder, P. H. L. Notten, *Adv. Mater.* **2011**, *23*, 4103.
[12] N. Sharma, M. V. Reddy, G. D. Du, S. Adams, B. V. R. Chowdari, Z. P. Guo, V. K. Peterson, *J. Phys. Chem. C* **2011**, *115*, 21473.
[13] W. S. Yoon, C. P. Grey, M. Balasubramanian, X. Q. Yang, J. McBreen, *Chem. Mater.* **2003**, *15*, 3161.
[14] W. S. Yoon, M. Balasubramanian, K. Y. Chung, X. Q. Yang, J. McBreen, C. P. Grey, D. A. Fischer, *J. Am. Chem. Soc.* **2005**, *127*, 17479.
[15] W. S. Yoon, K. Y. Chung, J. McBreen, K. Zaghib, X. Q. Yang, *Electrochem. Solid-State Lett.* **2006**, *9*, A415.
[16] N. E. Sung, Y. K. Sun, S. K. Kim, M. S. Jang, *J. Electrochem. Soc.* **2008**, *155*, A845.
[17] K. W. Nam, W. S. Yoon, K. Zaghib, K. Y. Chung, X. Q. Yang, *Electrochem. Commun.* **2009**, *11*, 2023.
[18] A. N. Mansour, F. Badway, W. S. Yoon, K. Y. Chung, G. G. Amatucci, *J. Solid State Chem.* **2010**, *183*, 3029.
[19] H. Tanida, H. Yamashige, Y. Orikasa, M. Oishi, Y. Takanashi, T. Fujimoto, K. Sato, D. Takamatsu, H. Murayama, H. Arai, E. Matsubara, Y. Uchimoto, Z. Ogumi, *J. Synchrotron Radiat.* **2011**, *18*, 919.
[20] S. W. Song, G. V. Zhuang, P. N. Ross, *J. Electrochem. Soc.* **2004**, *151*, A1162.
[21] J. T. Li, S. R. Chen, X. Y. Fan, L. Huang, S. G. Sun, *Langmuir* **2007**, *23*, 13174.
[22] S. F. Amalraj, D. Aurbach, *J. Solid State Electrochem.* **2011**, *15*, 877.
[23] D. Ostrovskii, F. Ronci, B. Scrosati, P. Jacobsson, *J. Power Sources* **2001**, *94*, 183.
[24] K. Dokko, M. Mohamedi, N. Anzue, T. Itoh, I. Uchida, *J. Mater. Chem.* **2002**, *12*, 3688.
[25] Y. A. Kim, M. Kojima, H. Muramatsu, S. Umemoto, T. Watanabe, K. Yoshida, K. Sato, T. Ikeda, T. Hayashi, M. Endo, M. Terrones, M. S. Dresselhaus, *Small* **2006**, *2*, 667.
[26] R. Imhof, P. Novak, *J. Electrochem. Soc.* **1999**, *146*, 1702.
[27] P. Novak, J. C. Panitz, F. Joho, M. Lanz, R. Imhof, M. Coluccia, *J. Power Sources* **2000**, *90*, 52.
[28] A. R. Armstrong, M. Holzapfel, P. Novak, C. S. Johnson, S. H. Kang, M. M. Thackeray, P. G. Bruce, *J. Am. Chem. Soc.* **2006**, *128*, 8694.
[29] C. P. Grey, N. Dupre, *Chem. Rev.* **2004**, *104*, 4493.
[30] B. Key, R. Bhattacharyya, M. Morcrette, V. Seznec, J. M. Tarascon, C. P. Grey, *J. Am. Chem. Soc.* **2009**, *131*, 9239.
[31] B. Key, M. Morcrette, J. M. Tarascon, C. P. Grey, *J. Am. Chem. Soc.* **2011**, *133*, 503.
[32] S. C. Chao, Y. C. Yen, Y. F. Song, Y. M. Chen, H. C. Wu, N. L. Wu, *Electrochem. Commun.* **2010**, *12*, 234.
[33] S. C. Chao, Y. F. Song, C. C. Wang, H. S. Sheu, H. C. Wu, N. L. Wu, *J. Phys. Chem. C* **2011**, *115*, 22040.
[34] D. Chen, S. Indris, M. Schulz, B. Gamer, R. Monig, *J. Power Sources* **2011**, *196*, 6382.
[35] J. Y. Huang, L. Zhong, C. M. Wang, J. P. Sullivan, W. Xu, L. Q. Zhang, S. X. Mao, N. S. Hudak, X. H. Liu, A. Subramanian, H. Y. Fan, L. A. Qi, A. Kushima, J. Li, *Science* **2010**, *330*, 1515.
[36] J. S. Weaving, F. Coowar, D. A. Teagle, J. Cullen, V. Dass, P. Bindin, R. Green, W. J. Macklin, *J. Power Sources* **2001**, *97–8*, 733.
[37] K. K. Lee, W. S. Yoon, K. B. Kim, K. Y. Lee, S. T. Hong, *J. Power Sources* **2001**, *97–8*, 308.
[38] H. Arai, S. Okada, Y. Sakurai, J. Yamaki, *Solid State Ionics* **1998**, *109*, 295.
[39] I. Belharouak, W. Q. Lu, D. Vissers, K. Amine, *Electrochem. Commun.* **2006**, *8*, 329.
[40] I. Belharouak, D. Vissers, K. Amine, *J. Electrochem. Soc.* **2006**, *153*, A2030.
[41] Y. D. Wang, J. W. Jiang, J. R. Dahn, *Electrochem. Commun.* **2007**, *9*, 2534.
[42] S. Muto, Y. Sasano, K. Tatsumi, T. Sasaki, K. Horibuchi, Y. Takeuchi, Y. Ukyo, *J. Electrochem. Soc.* **2009**, *156*, A371.
[43] D. P. Abraham, R. D. Twesten, M. Balasubramanian, J. Kropf, D. Fischer, J. McBreen, I. Petrov, K. Amine, *J. Electrochem. Soc.* **2003**, *150*, A1450.
[44] D. P. Abraham, R. D. Twesten, M. Balasubramanian, I. Petrov, J. McBreen, K. Amine, *Electrochem. Commun.* **2002**, *4*, 620.
[45] D. P. Abraham, J. Liu, C. H. Chen, Y. E. Hyung, M. Stoll, N. Elsen, S. MacLaren, R. Twesten, R. Haasch, E. Sammann, I. Petrov, K. Amine, G. Henriksen, *J. Power Sources* **2003**, *119*, 511.
[46] T. Ohzuku, Y. Makimura, *Chem. Lett.* **2001**, *30*, 642.
[47] K. M. Shaju, P. G. Bruce, *Adv. Mater.* **2006**, *18*, 2330.
[48] I. Belharouak, W. Q. Lu, J. Liu, D. Vissers, K. Amine, *J. Power Sources* **2007**, *174*, 905.
[49] Y. K. Sun, S. T. Myung, B. C. Park, J. Prakash, I. Belharouak, K. Amine, *Nat. Mater.* **2009**, *8*, 320.
[50] N. Yabuuchi, Y. T. Kim, H. H. Li, Y. Shao-Horn, *Chem. Mater.* **2008**, *20*, 4936.
[51] S. T. Myung, K. S. Lee, C. S. Yoon, Y. K. Sun, K. Amine, H. Yashiro, *J. Phys. Chem. C* **2010**, *114*, 4710.
[52] H. Konishi, T. Yuasa, M. Yoshikawa, *J. Power Sources* **2011**, *196*, 6884.
[53] W. S. Yoon, M. Balasubramanian, X. Q. Yang, J. McBreen, J. Hanson, *Electrochem. Solid-State Lett.* **2005**, *8*, A83.
[54] W. S. Yoon, K. Y. Chung, M. Balasubramanian, J. Hanson, J. McBreen, X. Q. Yang, *J. Power Sources* **2006**, *163*, 219.
[55] K. W. Nam, W. S. Yoon, X. Q. Yang, *J. Power Sources* **2009**, *189*, 515.
[56] K. K. Lee, W. S. Yoon, K. B. Kim, *J. Electrochem. Soc.* **2001**, *148*, A1164.
[57] K. K. Lee, W. S. Yoon, K. B. Kim, K. Y. Lee, S. T. Hong, *J. Electrochem. Soc.* **2001**, *148*, A716.
[58] Y. Kim, J. Eom, M. G. Kim, Y. K. Sun, C. S. Yoon, J. P. Cho, *J. Electrochem. Soc.* **2007**, *154*, A561.
[59] Y. Kim, Y. Hong, K. S. Ryu, M. G. Kim, J. Cho, *J. Power Sources* **2008**, *179*, 780.
[60] M. Guilmard, L. Croguennec, D. Denux, C. Delmas, *Chem. Mater.* **2003**, *15*, 4476.
[61] M. Guilmard, L. Croguennec, C. Delmas, *Chem. Mater.* **2003**, *15*, 4484.
[62] A. Debart, L. Dupont, P. Poizot, J. B. Leriche, J. M. Tarascon, *J. Electrochem. Soc.* **2001**, *148*, A1266.
[63] F. Wang, J. Graetz, M. S. Moreno, C. Ma, L. J. Wu, V. Volkov, Y. M. Zhu, *ACS Nano* **2011**, *5*, 1190.
[64] F. Wang, R. Robert, N. A. Chernova, N. Pereira, F. Omenya, F. Badway, X. Hua, M. Ruotolo, R. G. Zhang, L. J. Wu, V. Volkov, D. Su, B. Key, M. S. Whittingharn, C. P. Grey, G. G. Amatucci, Y. M. Zhu, J. Graetz, *J. Am. Chem. Soc.* **2011**, *133*, 18828.
[65] L. J. Wu, K. W. Nam, X. J. Wang, Y. N. Zhou, J. C. Zheng, X. Q. Yang, Y. M. Zhu, *Chem. Mater.* **2011**, *23*, 3953.
[66] G. G. Amatucci, J. M. Tarascon, L. C. Klein, *J. Electrochem. Soc.* **1996**, *143*, 1114.
[67] H. Arai, M. Tsuda, K. Saito, M. Hayashi, K. Takei, Y. Sakurai, *J. Solid State Chem.* **2002**, *163*, 340.
[68] S. C. Yin, Y. H. Rho, I. Swainson, L. F. Nazar, *Chem. Mater.* **2006**, *18*, 1901.
[69] J. J. Rehr, R. C. Albers, *Rev. Mod. Phys.* **2000**, *72*, 621.
[70] J. J. Rehr, A. L. Ankudinov, *Coord. Chem. Rev.* **2005**, *249*, 131.

[71] L. R. Sharpe, W. R. Heineman, R. C. Elder, *Chem. Rev.* **1990**, *90*, 705.
[72] S. Gross, M. Bauer, *Adv. Funct. Mater.* **2010**, *20*, 4026.
[73] M. G. Kim, C. H. Yo, *J. Phys. Chem. B* **1999**, *103*, 6457.
[74] M. G. Kim, H. J. Shin, J. H. Kim, S. H. Park, Y. K. Sun, *J. Electrochem. Soc.* **2005**, *152*, A1320.
[75] A. Y. Ignatov, N. Ali, S. Khalid, *Phys. Rev. B* **2001**, *64*, 014413.
[76] T. Yamamoto, *X-Ray Spectrom.* **2008**, *37*, 572.
[77] N. Kosugi, H. Kondoh, H. Tajima, H. Kuroda, *Chem. Phys.* **1989**, *135*, 149.
[78] W. S. Yoon, K. B. Kim, M. G. Kim, M. K. Lee, H. J. Shin, J. M. Lee, J. S. Lee, C. H. Yo, *J. Phys. Chem. B* **2002**, *106*, 2526.
[79] A. Manceau, A. I. Gorshkov, V. A. Drits, *Am. Mineral.* **1992**, *77*, 1133.
[80] Y. W. Tsai, J. F. Lee, D. G. Liu, B. J. Hwang, *J. Mater. Chem.* **2004**, *14*, 958.
[81] Y. W. Tsai, B. J. Hwang, G. Ceder, H. S. Sheu, D. G. Liu, J. F. Lee, *Chem. Mater.* **2005**, *17*, 3191.
[82] P. J. Chupas, M. F. Ciraolo, J. C. Hanson, C. P. Grey, *J. Am. Chem. Soc.* **2001**, *123*, 1694.
[83] P. J. Chupas, K. W. Chapman, C. Kurtz, J. C. Hanson, P. L. Lee, C. P. Grey, *J. Appl. Crystallogr.* **2008**, *41*, 822.
[84] B. Ravel, M. Newville, *J. Synchrotron Radiat.* **2005**, *12*, 537.